Univerza v Mariboru
Fakulteta za energetiko

Journal of ENERGY TECHNOLOGY

Volume 4 / Issue 2
MAY 2011
www.fe.uni-mb.si/si/jet.html

JOURNAL OF ENERGY TECHNOLOGY

VOLUME 4 / Issue 2

Revija Journal of Energy Technology (JET) je indeksirana v naslednjih bazah: INSPEC©, Cambridge Scientific Abstracts: Abstracts in New Technologies and Engineering (CSA ANTE), ProQuest's Technology Research Database.

The Journal of Energy Technology (JET) is indexed and abstracted in the following databases: INSPEC©, Cambridge Scientific Abstracts: Abstracts in New Technologies and Engineering (CSA ANTE), ProQuest's Technology Research Database.

JOURNAL OF ENERGY TECHNOLOGY

Revija JET je sofinancirana s strani Javne agencije za knjigo Republike Slovenije.

The Journal of Energy Technology is co-financed by the Slovenian Book Agency.

Jedrska energija po Fukušimi

Glede na naslov revije je nemogoče ne napisati nekaj misli o jedrski energiji po katastrofi v jedrski elektrarni Fukušima. Skoraj 25 let po jedrski katastrofi v Černobilu, ko si je javno mnenje o varnosti jedrskih objektov končno opomoglo, je to pridobljeno zaupanje odplavil cunami na severu Japonske. V času zmanjševanja uporabe fosilnih goriv zaradi vpliva na klimatske spremembe in zaskrbljenosti, da obnovljivi viri, kot sta sonce in veter, ne bodo zadostili potrebam po električni energiji, je jedrska energija izkazovala velik potencial. Ljudje se moramo zavedati, da je obnovljiva energija zelo draga, hkrati pa lahko za zadostno in stabilno proizvodnjo v bližnji prihodnosti izbiramo med dvema slabima opcijama: jedrsko ali nafto in premog.

Katastrofa v Fukušimi ima izredno velik vpliv na energijsko politiko. Če bo Nemčija nadaljevala z zapiranjem jedrskih elektrarn, se bo cena električne energije v Evropi zvišala. Ko je nemška vlada po katastrofi v Fukušimi zaprla sedem starih jedrskih elektrarn, se je Nemčija iz izvoznika električne energije (7000MW) spremenila v neto uvoznika (5000MW). V aprilu je Nemčija za pokrivanje razlike med proizvodnjo in porabo uvažala električno energijo iz Francije in Češke, ki 50 odstotkov električne energije proizvedeta v jedrskih elektrarnah.

Katastrofa v Fukušimi bo zelo vplivala na smernice razvoja tehnologij jedrskih elektrarn. Varnost bo najpomembnejša tema kupcev in razvijalcev opreme ne glede na ceno. Jedrska elektrarna v Fukušimi je v uporabi 41 let, kar pomeni, da je bila tehnologija razvita v 50-ih letih. Novejše tehnologije so bolj varne in učinkovite, kot tiste, ki so v elektrarnah, ki obratujejo. Tudi to je vzrok, da se obstoječe jedrske elektrarne posodabljajo in se njihova življenjska doba povečuje.

Izboljšanje varnosti gre v dve nasprotni smeri. Zasnova Areva, francoske jedrske velikanke (1650MW), z izboljšano varnostjo, ki prenese tudi letalsko nesrečo. Nasprotno, NuScale povezuje število majhnih jedrskih enot (45MW), podobno kot porazdeljeni računalniški sistemi v informacijskih tehnologijah. Majhne enote lahko za hlajenje uporabljajo konvekcijski sistem brez črpalk, kar je posebej zanimivo, saj je bilo neuspešno hlajenje s črpalkami glavni razlog za nesrečo v Fukušimi.

Naj zaključim s stavkom dr. Christophera Hooda, izvedenca in direktorja za japonske študije na Univerzi v Cardiffu: »Nihče ne zanika, ko ima jedrska energija slab dan ima res slab dan, vendar se moramo spomniti, ko imata plin in premog dober dan je to še vedno slab dan za okolje.«

Nuclear Power beyond Fukushima

In accordance to the title of the journal, it is impossible not to write some thoughts about nuclear power after the Fukushima disaster. Nearly 25 years after the Chernobyl nuclear disaster, the public perception of the safety of nuclear power had finally begun to recover; that confidence has been washed away by the tsunami in northern Japan. Between worries about the contribution of fossil fuel consumption to climate change and concerns that renewable energy supplies such as wind and solar cannot meet the world's needs for electricity, nuclear power seemed to be an obvious way forward. People have to realize that renewables cost a lot and that for stable energy production in near future we have to choose between two poor options: nuclear or oil and coal. The Fukushima disaster has had a huge impact on energy policy. If Germany continues shutting down all of its nuclear plants, electricity costs in Europe will rise. As the German government shutdown seven plants in response to the Fukushima disaster, Germany has turned from an exporter (7,000MW) to a net-energy importer (5,000MW). In April, Germany had to make up the difference with electricity from France and the Czech Republic, which produces about 50 percent of its power with nuclear energy.

The Fukushima disaster will change the direction of the development and design of nuclear plants. Safety has become the most important factor for buyers and designers. The Fukushima plant had been in operation for 41 years, which means that it was designed in the 1950s. The risks of next-generation plants are much lower than those of the plants now operating, and their efficiencies are much greater. This is the main reason that operating nuclear plants are continuously upgraded and their original projected life span is exceeded.

Improvements in safety go in two opposite directions. The design of Areva, the French (1,650MW) nuclear giant, has such enhanced safety that it is resistant even to planes crashing into it.

In contrast, NuScale reaches a greater scale by linking a number of very small units (45MW) in a manner similar to distributed computing in IT. The small unit is able to operate without pumps, using a convection-based cooling system, which is very attractive now, as the failure of water-cooling pumps was the major reason for the Fukushima disaster.

Let us conclude with Christopher Hood, an expert and director of the Japanese Studies Centre at Cardiff University: "There is no denying that when nuclear has a bad day it is a bad day, but you need to remember that when gas and coal have a good day it is still bad for the environment."

Krško, May 2011 Gorazd HREN

Table of Contents /
Kazalo

JET Volume 4 (2011), p.p. 11 - 20
Issue 2, May 2011
http://www.fe.uni-mb.si/si/jet.html

IMPROVING CENTRIFUGAL PUMP BY ADDING VORTEX ROTOR

IZBOLJŠANJE CENTRIFUGALNE ČRPALKE Z VORTEX ROTORJEM

Tihomir Mihalić[ℜ], Zvonimir Guzović, Stanislav Sviderek

Keywords: centrifugal vortex pump, hydrodynamic phenomena, energy transformation, unsteady flow, pump performance curves, energy efficiency, computational fluid dynamics.

Abstract

The changes of geological conditions of crude oil deposits and in the structure of layers, i.e. aging of drill wells, during the pumping of oil leads to a decrease in deposit pressure, as well as an increase in water, gas and the abrasive particle content in the pumped crude oil. At the same time, productivity is reduced; presently, over 60% of the world supplied oil is pumped with submersible centrifugal pumps powered by electric motors. Continuous improvement of their exploitation characteristics (e.g. flow (supply), pressure (head) and efficiency) is therefore necessary. Clearly such improvements can provide financial and energy savings, and thus have a positive impact on the environment, which is extremely important from the viewpoint of sustainable development. One experimentally and numerically verified method of improving the performance of centrifugal pumps is the method of creating a so-called coherent structure of eddies and turbulence in the peripheral area of the centrifugal vortex rotor mounted at the back side of centrifugal rotor. A new type of pump has been designed, called a "centrifugal vortex pump", which combines the benefits of these two types of pumps: a high value of the head of the vortex pump stage, and a high value of supply and high efficiency of centrifugal stage. Moreover, centrifugal pumps provide higher flow rates with lower pressure, while the vortex pumps give higher pressure, but with lower flow rates. Research on the energy transformations in the centrifugal vortex pump in this work was carried out using numerical simulations of the flow in the centrifugal pump, centrifugal vortex pump, the vortex part of the

[ℜ] Corresponding author: Tihomir Mihalić, PhD., Faculty of Mechanical Engineering and Naval Architecture, Zagreb, Tel.: +385 98 686 072, Fax: +385 1 616 8127, Mailing address: I.Lučića 5, Zagreb, Croatia
E-mail address: tihomir.mihalic@fsb.hr

centrifugal vortex pump, and also by taking measurements of relevant parameters that describe the performance of pumps at their physical models. The measurement results were used as experimental validation of numerical simulations; vice versa, flow visualization derived from the numerical simulation was used to interpret measurements. An assessment of vortex rotor contribution on the head of centrifugal vortex pump was made. The influence of the vortex rotor on the efficiency of the centrifugal vortex pump was compared to a centrifugal pump with the same geometry. In order to better understand the energy transformations that are the result of interaction between the flow from the channels of centrifugal part of centrifugal vortex rotor and vortices formed at the vortex part of centrifugal vortex rotor and their interactions with the stator, an analysis of the structure of flow was conducted.

Povzetek

Spremembe geoloških pogojev in strukture plasti nahajališč surove nafte, kot so staranje vrtin med črpanjem nafte, vodijo k zmanjšanju tlaka v nahajališču ter k povečanju vsebnosti vode, plina in abrazivnih vključkov med črpanjem surove nafte. Hkrati se produktivnost črpanja manjša, tako se dandanes več kot 60% črpanja nafte izvaja s potopnimi črpalkami, ki jih poganjajo elektromotorji. Zato je razumljiva tendenca k nenehnim izboljševanjem potopnih črpalk, njihovih »*produkcijskih*« karakteristik kot so tok (dotok), tlak (glava) in učinkovitost. Izboljšave omogočajo večjo ekonomičnost in energijsko varčnost in posledično pozitivno vplivajo na okolje, kar je pomembno pri trajnostnem razvoju energetike. Eden od načinov izboljšave delovanja centrifugalnih črpalk je uvedba tako imenovanih koherentnih strukturnih vrtincev in turbulence v okoliškem področju, dodanih na koncu rotorja, kar je že potrjeno z eksperimenti in numerično. Zasnovan je nov tip črpalke, imenovan centrifugalna vrtinčna črpalka, ki združuje prednosti dveh črpalk, in sicer visoko vrednost vrtinčne stopnje in visoko učinkovitost centrifugalnega dela. Centrifugalne črpalke zagotavljajo višjo stopnjo pretoka pri nižjem tlaku, vrtinčne črpalke pa višji tlak pri nižji stopnji pretoka. Raziskava energijskih transformacij v centrifugalni vrtinčni črpalki, opisani v tem članku, je bila izvedena z numeričnimi simulacijami toka v centrifugalni črpalki, centrifugalni vrtinčni črpalki in posebej v vrtinčnem delu centrifugalne vrtinčne črpalke. Izvedene so bile meritve relevantnih parametrov in učinkovitosti črpalke na fizičnem modelu. Rezultati meritev so bili uporabljeni kot eksperimentalna potrditev numeričnih simulacij in obratno, vizualizacija tokov numerične simulacije je bila uporabljena za razlago meritev. Izvedena je bila ocena prispevka vrtinčnega dela rotorja na glavi črpalke. Vpliv vrtinčnega dela rotorja na učinkovitost vrtinčne črpalke je primerjan s centrifugalno črpalko enake geometrije. Za boljše razumevanje energijskih transformacij, ki so posledica interakcije med tokom iz kanalov centrifugalnega dela centrifugalnega vrtinčnega dela rotorja in vrtincev na vrtinčnem delu centrifugalnega vrtinčnega rotorja ter hkratne interakcije s statorjem, je bila izvedena tudi analiza strukture toka.

1 INTRODUCTION

One way of improving the characteristics of centrifugal pumps is adding a vortex rotor to the centrifugal rotor by which energy of induced vortices at the vortex rim is added to fluid energy gained in centrifugal rotor, Mihajlovič [1], Isaakovič [2], Karakulov [3], Eriberto [4], Figure 1.

Figure 1: *Centrifugal vortex pump stage*

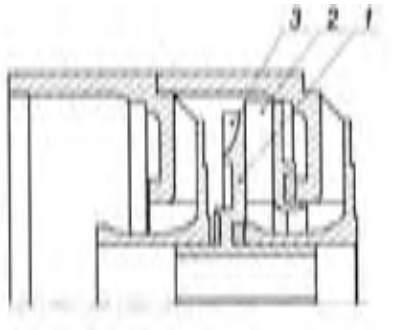

Figure 2: *Cross section of the centrifugal vortex pump stage*

Figure 2 shows a cross-section of the centrifugal vortex pump stage with annotated major components. On the periphery of the disc (1) of the centrifugal rotor (2) on the stator side, the vortex rim (rotor) is installed (3). There is a certain gap between the stator cover and vortex radial vanes. This gap, together with the gap between centrifugal vanes and the stator entrance, forms a peripheral-lateral annular vortex chamber.

The resulting additional kinetic energy of coherent structures induced at the vortex rim transforms to the head H_4, which is added to the bulk head (pressure) obtained in the centrifugal rotor of the centrifugal vortex pump.

$$H = H_{cen} + H_4 \tag{1.1}$$

Mere physical simulations (experiments) do not provide the necessary information about the structure of the energy conversions. Therefore, the use of the joined method, computers simulations (CFD) together with experiment, can provide insight into the structure of flows and the quantification of parameters, which helps in understanding the processes of energy conversions.

---

2 NUMERICAL MODEL OF CENTRIFUGAL VORTEX PUMP

Numerical simulations of unsteady flow in centrifugal pumps, centrifugal vortex pumps and vortex pumps were carried out using ANSYS Fluent software. The simulation includes a whole centrifugal and centrifugal vortex pump stage, including suction and discharge pipe (*Figure 3)*. Between physical and numerical models, geometric, kinematic and dynamic conditions for similar work were satisfied. A simplification of geometries has been conducted only in areas that do not affect the flow in the stator and rotor.

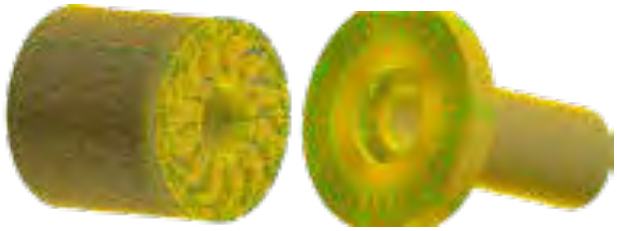

Figure 3: *Control volume mesh of centrifugal vortex pump stage*

On the left side of Figure 3, the discretized stator with the outlet is shown, while the discretized rotor inlet pipe is shown on the right is shown.

In the CFD model, the rotor rotates freely, and is connected to the rest of the domain with a sliding mesh boundary condition. Calculation of the rotor, Figure 4, takes place in a non-inertial, rotating coordinate system. The output tube is connected with the output from the stator with the interface boundary condition in order to discretize it with larger control volumes of those by which stator is discretized, Figure 5, because there the flow is less demanding for simulation than the flow in the stator and rotor.

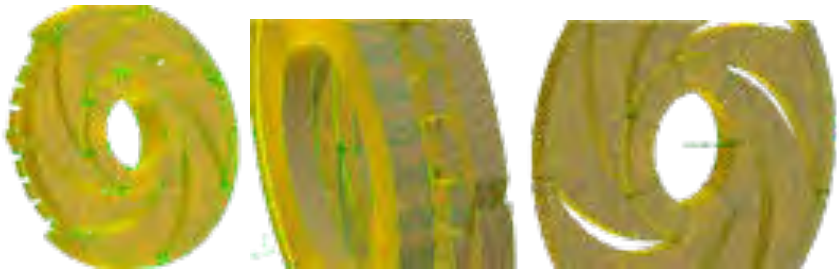

Figure 4: *Structured mesh of rotor*

Figure 5: *Structured mesh of rotor*

The entire continuum is discretized with three meshes of control volumes. The first mesh consists of 962,159 control volumes and 108,640 nodes, with the greatest control volume edge of 0.5 mm; the second one consists of 1,864,399 control volumes and 2,007,183 nodes, with the greatest control volume edge of 0.4 mm; the third mesh consists of 3,340,658 control volumes and 3,573,140 nodes with the greatest control volume edge of 0.3 mm. Of the total number of control volumes, 85% of them were hexahedral control volumes, and 15% were mixed control volumes.

Given that the research was conducted at the rotor angular speed n = 2910 min^{-1}, simulations were performed with a time step of 8×10^{-5} s. The time step was chosen after research for a suitable time step with respect to convergence. Within the one-time step, the rotor is turned by 1.5°. The selected time step showed rapid convergence solutions. For the working fluid, water of standard properties at 25°C was used.

Turbulence was modelled using a hybrid DES SST model (detached eddy simulations).

Boundary conditions were set far enough from the stage so that their impact on the flow could be ignored. At the entrance to the domain, a pressure-inlet boundary condition has been used, while at the exit from the domain, an outlet-vent boundary condition has been used, because it allows adjustment of the loss coefficient at the exit.

Boundary condition outlet vent is defined by pressure loss (attenuation) that is proportional to dynamic pressure:

$$\Delta p = k_L \frac{1}{2}\rho v^2 \tag{2.1}$$

Boundary condition outlet vent was also chosen because it best describes the physics of this research, where the flow is regulated by the valve at the exit, from fully open to fully closed. Loss coefficient k_L in the boundary condition outlet vent (2.1) is a number, and the whole simulation was conducted with k_L = 0 (fully open valve), 2, 5, 10, 20, 60, 300 (fully closed valve), Fluent user guide [5].

3 EXPERIMENTAL MODEL OF CENTRIFUGAL VORTEX PUMP

The rotor and stator, formed from transparent plexiglass, are also embedded in a transparent casing of plexiglass to enable flow visualization, both in the passages of the rotor and the stator and in the zone of special interest for research, i.e. the chamber between the rotor and the stator, where the case of the centrifugal vortex pump vortex rim is a located, Figure 6.

Figure 6: *Centrifugal and centrifugal vortex pump stage made of Plexiglas for experimental research*

Experimental assembly, Figure 7, starts with a valve at the entrance, followed by a 1-m-long tube of Plexiglas, a venturi tube, a 1-m-long tube of plexiglas with measuring points for measuring pump suction pressure, then the metering section containing various pump stages is installed, following a 1-m-long tube of plexiglas with the measuring points for measuring pump discharge pressure and the outlet valve. Valves are used for regulating measurements. The experimental assembly is made in accordance with the following standards: ISO 5167-1,2,3, 4:2003 and ISO / TR 15377:2007.

Figure 7: *Experimental assembly*

4 VALIDATION OF THE USED NUMERICAL MODEL

Figure 8 shows the process of validation of the numerical solutions for *Q-H* characteristic of the centrifugal vortex pump stage. Validation is performed by comparing numerical solutions with experimental solution.

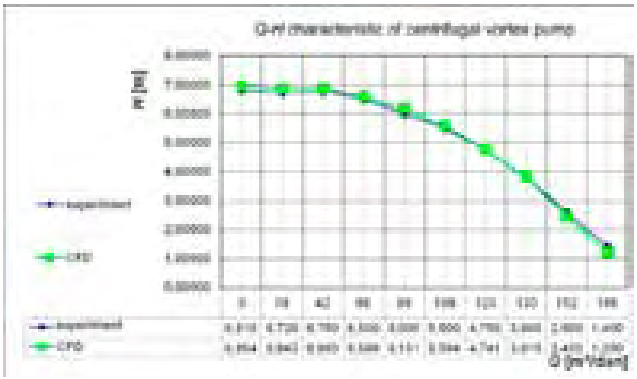

Figure 8: *Comparison of Q-H characteristics of centrifugal vortex pump stage, obtained by CFD and experiment, n= 2910 min-1*

Figure 8 shows very good agreement of CFD results with experimental results. It is evident that the CFD in the zone from the 165 m³/day (1.91 l/s) to 123 m³/day (1.42 l/s) fall short in comparison to the experiment, which is attributed to the lack of used computational domain. When k_L = 0, the pump generates *H* = 3.81565 m, which shows that the output from the domain is too small (too small a cross section) for the generated flow.
In order to numerically calculate *Q-H* points below the *H* = 3.81565 m, the exit of the domain boundary condition was changed by reducing the default value for the pressure loss of flow that occurs due to a small section of the output. Flow rate of 108 m³/day (1.25 l/s) to 0 m³/day CFD solution exceeded the experimental solution, which is an error of computational simulation that has been reported in Launder [6]. According to the Feng [7], CFD fall short in predicting the intensity of turbulence, but it generates higher velocity fields in the radial space between the rotor and stator (diffuser). Since this space is of crucial importance for the centrifugal vortex pump, this is a valid explanation for the larger *H* in this range of the flow. Specifically, generated flow with these higher velocity fields encounters the vortex rim, which then generates more energy, so fluid with increased energy enters the diffuser, which then generates higher H_4 according to Equation (1.1), resulting in higher *H*.
However, since the maximum deviation of head is 0.15 m with a flow rate of 89 m^3/day (1.03 l/s), which was 2.5% of the head at that flow, and since the average deviation of head throughout the whole working scope was 0.09 m, the CFD solution is considered that has well-described covered physics of current flow.

5 RESULTS OF THE NUMERICAL AND EXPERIMENTAL RESEARCH OF CENTRIFUGAL VORTEX PUMP

5.1 Comparison of *Q-H* characteristic of centrifugal and centrifugal vortex pump

Figure 9 shows the *Q-H* characteristics of a centrifugal pump stage and the *Q-H* characteristics of a hybrid centrifugal vortex pump stage. It is evident that the characteristics of the centrifugal vortex pump smoothly follow the characteristics of centrifugal pump from the maximum flow to the flow of 105 m^3/day (1.22 l/s). After the flow of 105 m^3/day (1.22 l/s), the characteristics of

---

the centrifugal vortex pump continue to rise steeply as a characteristic of vortex pumps in Dochterman [8], opposed to the characteristics of centrifugal pump, which grows slower than the characteristics of the centrifugal vortex pump to its maximum at flow rate of 65 m³/day (0.75 l/s), and then begins to decline steeply. This form of performance curve (falling steeply after its maximum) represents the instability of the pump, because the pump can generate two different flow rates at a given head, left and right from the maximum *Q-H* characteristic curve, Lobanoff [9].

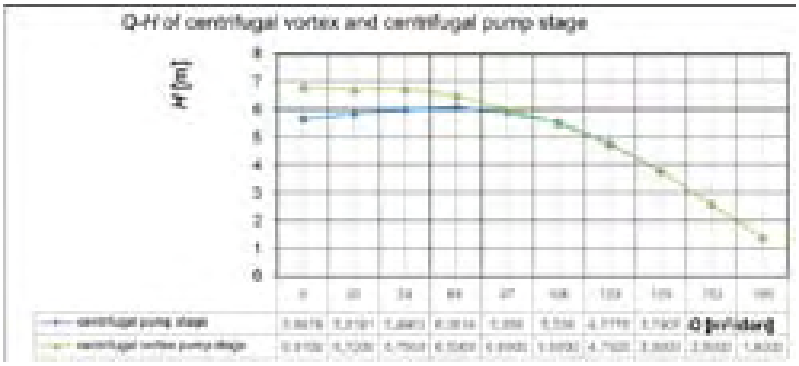

Figure 9: *Comparison of Q-H characteristics of centrifugal vortex and centrifugal pump stage, n= 2910 min-1*

Adding a vortex rotor to the centrifugal pump stage provided a steeply sloping *Q-H* characteristic pump, which ensures the stability of its operation. This confirmed one of the positive roles of the vortex rim in the centrifugal vortex pump stage.

5.2 Quantification of the portion of head generated by vortex rotor in the head of centrifugal vortex pump

The contribution of eddy processes on the amount of the head and the corresponding increase in pressure depends on the flow rate and the given flow rate depends on the magnitude of the axial component of absolute velocity of the fluid from the discharge of centrifugal rotor to the entrance in the diffuser channels. The lower the flow rate and the smaller the axial velocity component are, the greater the number of the vortex rim passages participating in the change of momentum between the fluid contained in these passages at that instant of time and the main stream of the fluid from the centrifugal rotor to the diffuser.

Figure 10 clearly shows that the vortex rim in the centrifugal vortex pump stage begins to increase the amount of the head from the flow rate of 105 m³/day (1.22 l/s) to the zero flow rate, which is very convenient, because if there is a higher demand on the pump, as to overcome the greater resistance, the vortex rim is increasingly helping the pump.

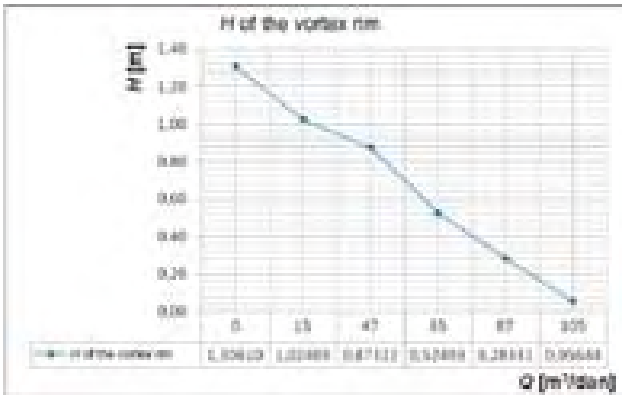

Figure 10: *Contribution of the energy fluxes from the vortex rim to the increase of head H, n= 2910 min-1*

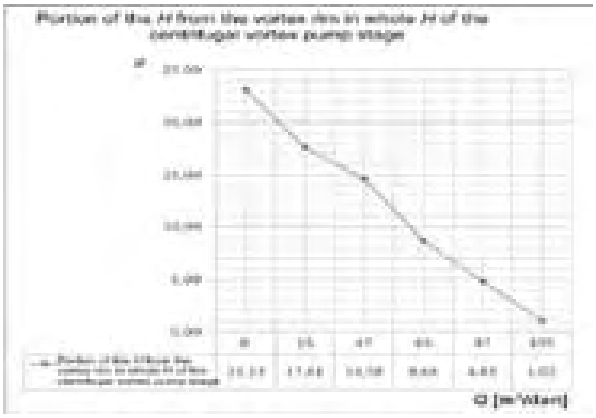

Figure 11: *Portion of the head generated by vortex rim in the whole head of the centrifugal vortex pump stage, n= 2910 min-1*

The swirl effect achieved by vortex rim increased the magnitude of the head for a maximum of 23.13% (average increase of 11.64%) is shown in Figure 11.

6 CONCLUSION

This work has proven and quantified the benefits of the centrifugal vortex pump stage in relation to the centrifugal one. The method used was based on the unsteady CFD experiments and experiments on physical models. Detailed measurements on physical models of the power consumed to drive the centrifugal and the centrifugal vortex pump stage resulted in more accurate quantification of energy balance.

It was proven that the kinetic energy of coherent vortex structures created by the vortex rim is added to the fluid flowing from the passages of the centrifugal rotor and thus increases the total energy of the fluid before entering the stator. Furthermore, this extra energy is added to the main fluid stream by the longitudinal vortices generated by the edges of the vortex rim due to a change of kinetic energy of eddies and by the radial vortices detached off vortex rim vanes.

In further research, the effect of adding the vortex rim to the centrifugal pump stage to the cavitation and efficiency should to be investigated. It is necessary to carry out a detailed study of the impact of the shape of the vortex rim vanes and of the dimensions of the vortex chamber on the characteristics of the centrifugal vortex pump.

References

[1] **Mihajlovič, P. O., Jurevič, M. I., Borisovič, K. P., Isaakovič, R. A., Pavlovič, T. I.:** *New rotary-vortex pumps for crude oil production in the complicated conditions*, 1. Međunarodna naučno-tehnička konferencija, Rusija, Voronež, 17-22 rujna 2001.

[2] **Isaakovič, R. A, Vasiljevič, G. N.:** *High-head, economical modification of multistage centrifugal pump for oil production*, 2. Međunarodna naučno-tehnička konferencija, Rusija, Voronež, 15-20 rujna 2003.

[3] **Karakulov, S. T., Meljnikov, D. J., Pereljmman, M. O., Dengaev, A. V.:** *Ob odnoj vozmožnosti povišenija effektivnosti ekspluataciji gazonasiščennih skvažin*, 3. Međunarodna naučno-tehnička konferencija, Rusija, Voronež, 14-17 rujna 2005.

[4] **Melzi, Eriberto**: *Vortex impeller for centrifugal fluid-dynamic pumps*, European Patent Application EP1 961 965 A2, Italija, 2008.

[5] **Fluent Inc**: *Fluent 12 user guide*, Fluent Inc.,

[6] **Launder, B.E., Spalding, D.B.**: *Lectures in Mathematical Models of Turbulence*, Academic Press, London, 1972. [65] BE oprati, DB Spalding, Predavanja u Matematičko modeliranje turbulencije, Academic Press, London, 1972.

[7] **Feng, J., Benra, F.K. and Dohmen, H.J.**: *Comparison of Periodic Flow Fileds in a Radial Pump among CFD, PIV and LDV Results*, International Journal of Rotating Machinery, Volume 2009

[8] **Dochterman, R. W., General Electric Company:** *Centrifugal-vortex pump*, United States Patent 3,936,240, USA, 1974.

[9] **Lobanoff, V.S., Ross, R.R.:** *Centrifugal pumps – Design & Application*, 2nd edition, Butterworth-Heinemann, USA, 1992

Nomenclature

H	head
Q	flow rate
n	angular velocity

JET Volume 4 (2011), p.p. 21-30

Issue 2, May 2011

http://www.fe.uni-mb.si/si/jet.html

INFLUENCE OF THE TURBULENCE MODEL ON THE NUMERICAL PREDICTIONS OF THE CAVITATING FLOW AROUND A HYDROFOIL

VPLIV TURBOLENTNEGA MODELA NA NUMERIČNO NAPOVED KAVITACIJSKEGA TOKA OKROG HIDROPROFILA

Mitja Morgut[ℜ], Enrico Nobile[1]

Keywords: RANS, turbulence model, cavitation, NACA66(MOD)

Abstract

In this paper, the influence of the turbulence model on the numerical predictions of the cavitating flow around a hydrofoil is investigated. The flow is modelled using the RANS (Reynolds Averaged Navier-Stokes) approach in combination with the interphase capturing VOF (Volume of Fluid) method. The study is carried out considering the cavitating flow around the NACA66(MOD) hydrofoil at two angles of incidence and employing three widespread turbulence models. The numerical results show that the turbulence model may play a minor role for the prediction of the stable sheet cavity flow over a hydrofoil.

Povzetek

V tem članku opisujemo raziskavo vpliva turbulentnega modela ob numeričnih predpostavkah na kavitacijo v toku ob hidravličnem profilu. Za modeliranje toka je uporabljen RANS pristop v kombinaciji z medfaznim zajemanjem končnih volumnov toka (VOF). Študija zajema kavitacijski

[ℜ] Mitja Morgut, Dipartimento di Ingegneria Meccanica e Navale, University of Trieste, Trieste, Italy, Tel.: +39 040 558 3502, Fax: +39 040 572 033, E-mail address: mmorgut@units.it

[1] Prof. Enrico Nobile, Dipartimento di Ingegneria Meccanica e Navale, University of Trieste, Trieste, Italy, Tel.: +39 040 558 3507, Fax: +39 040 572 033, E-mail address: nobile@units.it

---

tok okrog hidravličnega profila oblike NACA66(MOD) pri dveh nastavnih kotih in upošteva tri znane modele turbulence. Rezultati numeričnih analiz kažejo, da je za napoved stabilnega kavitacijskega toka ob hidravličnem profilu, turbulentni model manjšega pomena.

1 INTRODUCTION

Cavitation is a phenomenon that consists of the formation and activity of bubbles (or cavities) in a liquid, [1]. It occurs in many liquids when the local pressure is decreased below a certain value. However, it is mainly observed in water, because most of devices use tap water as working liquid.

Cavitation is important due to its effects that can be desirable or undesirable. In most cases, however, the effects produced by cavitation are undesirable. In the field of applied hydraulics, the negative effects of cavitation usually occur in turbines, pumps, propellers, pipe systems, valves etc. In such systems, cavitation affects the hydrodynamic of the flow field negatively and can produce excessive noise, vibrations and surface erosion. The negative modifications of the flow field can lead, for instance, to considerable head losses in pumps and to a decrease in both power output and efficiency in hydraulic turbines. However, in order to avoid overly conservative designs, increasing effort is directed towards designing in order to avoid the consequences of cavitation, while allowing the phenomenon to exist, [2].

For these reasons, contemporary CFD (Computational Fluid Dynamics) technologies, which enable the prediction of the global characteristics and also provide detailed descriptions of the flow field of a given system/device are currently routinely used during the design process. However, the accuracy of the numerical predictions can be affected by several factors.

In this paper, the influence of the turbulence model on the numerical predictions of the cavitating flow around a NACA66(MOD) hydrofoil is investigated. We considered three standard, widely used two-equation turbulence models, i.e. k-ε, RNG k-ε and the SST (Shear Stress Transport) model. The simulations were carried out using the ANSYS-CFX 12.1 commercial CFD solver. From the computational results, it seems that for the prediction of the stable sheet cavity flow over the hydrofoil, the different turbulence models considered in this work can guarantee similar levels of accuracy.

In the following, the mathematical model is presented first, followed by the descriptions of the test case and the simulation strategy. Then the preliminary studies and the collection of significant results for both non-cavitating and cavitating flow conditions are provided. Our concluding remarks are then given.

2 MATHEMATICAL MODEL

In this paper, the cavitating (and non-cavitating) flow was simulated using the RANS (Reynolds Averaged Navier-Stokes) approach in combination with the homogeneous multiphase transport equation based model, [3].

In ANSYS-CFX 12.1 using the homogeneous multiphase transport equation-based model, the cavitating flow can be modelled as a mixture of two species, i.e. vapour and liquid behaving as one, and can be described with the following set of governing equations for our problem.

$$\begin{cases} \nabla \cdot \boldsymbol{U} = \dot{m}\left(\frac{1}{\rho_l} - \frac{1}{\rho_v}\right) \\ \frac{\partial(\rho \boldsymbol{U})}{\partial t} + \nabla \cdot (\rho \boldsymbol{U}\boldsymbol{U}) = -\nabla P + \nabla \cdot [(\mu + \mu_t)(\nabla U + (\nabla U)^T)] \\ \frac{\partial \gamma}{\partial t} + \nabla \cdot (\gamma \boldsymbol{U}) = \frac{\dot{m}}{\rho_l} \end{cases} \tag{2.1}$$

Phases are considered incompressible and share the same instantaneous velocity $\boldsymbol{U}$ and pressure fields P. Moreover, in the above equations, which are (in order) the continuity and the momentum equation for the liquid-vapour mixture, the liquid volume fraction equation $\dot{m}$ (kg/m^{3}s) is the interphase mass transfer rate due to cavitation, ρ_v(kg/m^3) the vapour density, ρ_l(kg/m^3) the liquid density, and μ_t (kg/m s) is the turbulent viscosity. The water volume fraction, γ, and the vapour volume fraction α are defined as follows:

$$\gamma = \frac{volume\ liquid}{total\ volume} \qquad \alpha = \frac{volume\ vapour}{total\ volume} \tag{2.2}$$

and are related to each other through the following relevant constitutive relation

$$\gamma + \alpha = 1 \tag{2.3}$$

Finally, ρ (kg/m^3) and μ (kg/m s) are the density and the dynamic viscosity of the vapour-water mixture, scaled by the water volume fraction, respectively.

$$\begin{cases} \rho = \gamma \rho_l + (1 - \gamma)\rho_v \\ \mu = \gamma \mu_l + (1 - \gamma)\mu_v \end{cases} \tag{2.4}$$

To close the set of the governing equations, an additional modelling is required in order to evaluate the turbulent viscosity and the interphase mass transfer rate due to cavitation.

As previously anticipated, in this work, the turbulent viscosity was computed using three different two-equation turbulence models, i.e. k-ε, RNG k-ε and the SST model. The k-ε and RNG k-ε models were used in combination with the scalable wall functions. The SST model was used, employing the automatic wall treatment. For a detailed description of the above models, please see [4, 5].

The mass transfer rate due to cavitation was computed using the mass transfer model known as the *full cavitation model*. This model was originally presented in [6]. It was derived on the basis of the Rayleigh-Plesset equation for bubble dynamics, and its formulation is stated as follows, where f_v is the vapour mass fraction, k (m^2/s^2) is the turbulent kinetic energy, T (N/m) is the surface tension, and C_e and C_c are two empirical calibration coefficients.

$$\dot{m} = \begin{cases} -C_e \frac{\sqrt{k}}{T} \rho_l \rho_v \sqrt{\frac{2}{3}\frac{P_v - P}{\rho_l}} \left(1 - f_v\right) & if\ P < P_v \\ C_c \frac{\sqrt{k}}{T} \rho_l \rho_l \sqrt{\frac{2}{3}\frac{P - P_v}{\rho_l}} f_v & if\ P > P_v \end{cases} \tag{2.5}$$

For convenience, in this study the formulation proposed by [7] was used, in which the vapour mass fraction, f_v, was replaced by the vapour volume fraction α. Moreover, in order to improve the accuracy of the simulations, the empirical coefficients (C_e, C_c) were previously properly calibrated for the prediction of the cavitating flow around a hydrofoil, [8].

3 TEST CASE

The NACA66(MOD) hydrofoil, used as a test case, was designed with a camber ratio of f/c=0.020, a NACA meanline of *a=0.8* and a thickness ratio of *t/c=0.9*, where *f* was the maximum thickness, *t* the maximum camber and *c* the chord length of the hydrofoil section. The experimental measurements were carried out in the High-Speed Water Tunnel of the California Institute of Technology, [9]. The hydrofoil used in our simulations was completely smooth and had a chord of *c=150 mm*.

4 SOLUTION STRATEGY

To investigate the flow around the NACA66(MOD) hydrofoil, we used the computational domain, as shown in Figure 1, and set the boundary conditions as described in the following. The simulations were carried out in 2D and in steady-state conditions.

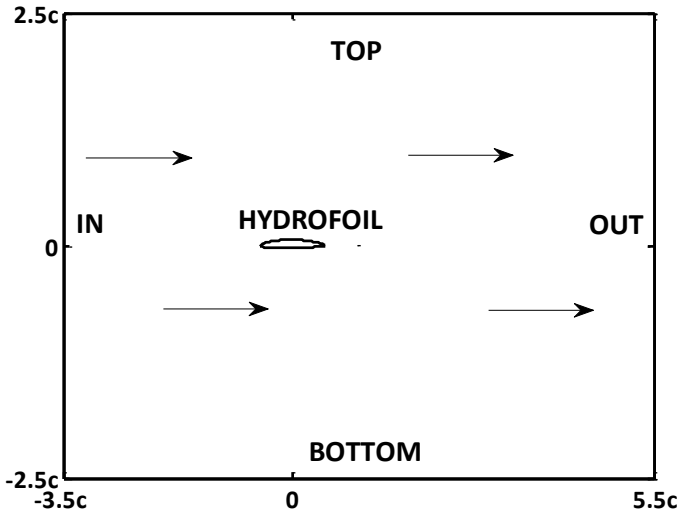

Figure 1: *Geometry of the computational domain and boundary conditions*

4.1 Boundary Conditions

On solid surfaces (HYDROFOIL, TOP, BOTTOM), the velocity no-slip condition was applied. On the outlet boundary (OUT), a fixed static pressure, P_{ref}=202650 Pa was imposed; on the side surfaces, the symmetry condition was enforced. On the inlet boundary (IN), the values of the free stream velocity components and turbulence quantities were fixed. Moreover, water and vapour volume fractions were set equal to 1 and 0, respectively. In order to match the experimental setup, the same Reynolds numbers were used in the numerical investigations.

Since the water used in simulations had a fixed density ρ_l=998 kg/m^3 with a kinematic viscosity of v_l=8.92x10^{-7} m/s, the free-stream velocity was fixed equal to U=12.2 m/s. The vapour density was also kept constant and equal to ρ_v= 0.02308 kg/m^3. Finally, assuming a turbulent intensity of 1% at the inlet, the turbulent kinetic energy and the turbulent dissipation rate were set equal to k = 0.0223 (m^2/s^2) and ε = 0.1837 (m^2/s^3), respectively**.**

Different cavitating flow regimes related to the cavitation number σ were defined varying the value of the saturation pressure P_v. This because P_{ref}, U, ρ_l were kept constant and σ was defined as:

$$\sigma = \frac{P_{ref} - P_v}{(1/2)\rho_l U^2} \tag{4.1}$$

4.2 Meshing

All the meshes used in this study were hexa-structured with an average value of y^+ equal to 23 on the solid surfaces of the hydrofoil, evaluated at an angle of attack of *AoA=4°.* It was defined as $y^+=\mu_\tau y/v$, where $\mu_\tau=(\tau_\omega/\rho_l)^{1/2}$ was the friction velocity, y the normal distance from the wall, v the kinematic viscosity, τ_ω the wall shear stress. They were constructed using the ANSYS-ICEM CFD 12.1 meshing tool. For illustration purposes, Figure 2 shows the blocking structure around the hydrofoil and the computational grid corresponding to the mesh, which will be identified as mesh B in the following.

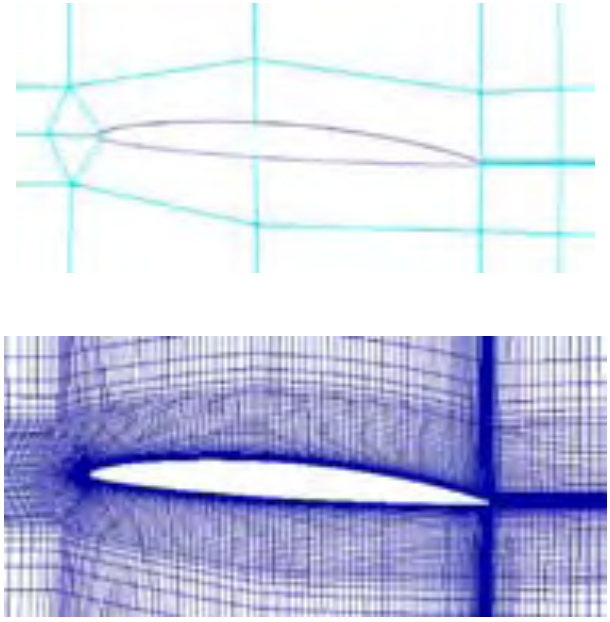

Figure 2: *Blocking (top) and mesh B (bottom) around the hydrofoil*

---

5 PRELIMINARY INVESTIGATIONS

Before investigating the influence of the different turbulence models on the numerical predictions of the cavitating flow around the NACA66(MOD) hydrofoil, we investigated the influence of the mesh resolution. This study was carried out in non-cavitating conditions by monitoring the influence of three progressively finer meshes (A, B, C) on the values of the lift C_L and drag C_D coefficients, and also on the minimum value of the pressure coefficient $C_{P,min}$ defined as follows:

$$C_L = \frac{F_L}{(1/2)\rho U^2 S} \qquad C_D = \frac{F_D}{(1/2)\rho U^2 S} \qquad -C_P = \frac{P_{ref} - P}{(1/2)\rho U^2 S} \tag{5.1}$$

In the above equations, $S=c \cdot d$ is the planar surface with d equal to the span. Simulations were carried out using the k-ε turbulence model. Moreover, during the mesh refinement the distances of the first nodes from the solid surfaces were the same for all the meshes. This allowed us to keep the numerical model, in particular the turbulence wall model, unchanged and thus perform a consistent mesh independence study. From the results collected in Table 1, it is possible to see that the results obtained with finer meshes, i.e. mesh B and mesh C, were very close to each other. For this reason, we decided to carry out the rest of the simulations using mesh B. For comprehensiveness, Figure 3 shows the pressure distribution over the suction side of the hydrofoil obtained using the different resolution meshes.

Table 1: *Results of the Mesh independence study*

ID Mesh	*Resolution*	*Nodes*	C_L	C_D	$C_{P,\,min}$
A	Coarse	30504	0.650	0.015	1.92
B	Mid	58734	0.649	0.017	1.75
C	Fine	122380	0.648	0.017	1.73
Exp.			0.629	0.018	1.76

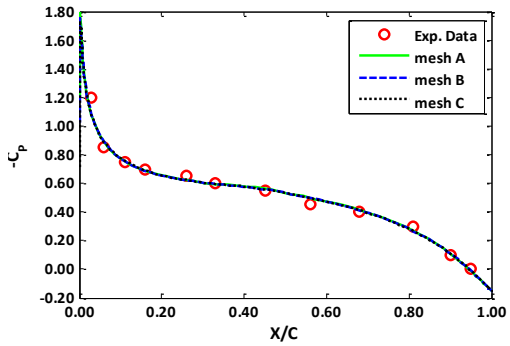

Figure 3*: Pressure distributions along the suction side of the hydrofoil. Simulation were carried out at AoA=4°, Re=2x10^6 using the k-ε turbulence model.*

6 COMPARISON OF DIFFERENT TURBULENCE MODELS

In the following, we first present a selection of the result obtained for the non-cavitating flow conditions followed by the results obtained for different cavitating flow regimes. In both cases, we investigated the flow considering two different angles of attack: *AoA=4°* and *AoA=6°.*

6.1 Fully Wetted Flow

For the fully wetted flow conditions in Figure 4, we present the pressure distributions over the suction side of the hydrofoil computed at *AoA=4°.* From Figure 4 (left), it is possible to see how the pressure distributions along the hydrofoil computed with different turbulence models were in line with each other. However, from Figure 4 (right) it is interesting to note that in the proximity of the leading edge region, the pressure distribution computed with the standard *k-ε* model differed from those computed with the other two models. Similar trends were also observed for the case of *AoA=6°.* This incongruence in pressure distributions, may partially justify the differences in the results obtained in the following cavitating flow conditions.

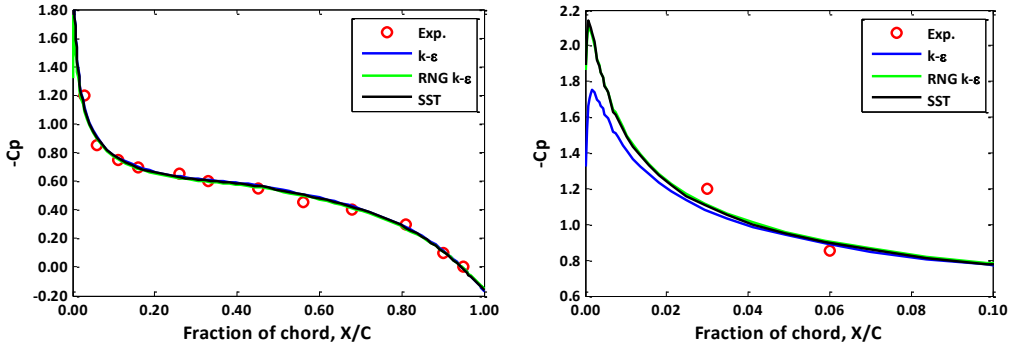

Figure 4: Pressure distributions along the suction side of the hydrofoil. Simulations were carried out at *AoA=4°, Re=2x10*^{6} using three different turbulence models.

6.2 Cavitating Flow

From the results collected in the following Tables 3 and 4, it is possible to note that for both angles of incidence the results obtained with the different turbulence models were in line with the experimental data, even though for more severe cavitating flow regimes the numerical predictions seem to under-predict both lift and drag forces. The results obtained with different turbulence models were very close to each other, even though when using the *k-ε* model the values of C_L and C_D were respectively lower and higher of those obtained with the other two models. Next, Figures 5 and 6 show the pressure distributions over the suction side of the hydrofoil, confirming the good congruency between the results obtained with different models. Appreciable differences were observed only at an incidence of four degrees, where the bubbles predicted using the *k-ε* model were less diffused (at the closure region) than those obtained with other two models, as qualitatively shown in Figure 7.

Table 2: *Results obtained for AoA = 4 ° at Re=2x10^6 using different turbulence models*

	C_L				C_D			
σ	***Exp***	***k-ε***	**RNG *k-ε***	***SST***	***Exp***	***k-ε***	**RNG *k-ε***	***SST***
1.00	0.645	0.654	0.659	0.656	0.020	0.017	0.014	0.013
0.91	0.670	0.664	0.672	0.667	0.021	0.018	0.014	0.014
0.84	0.699	0.674	0.686	0.688	0.024	0.021	0.015	0.015

Table 3: *Results obtained for AoA = 6 ° at Re=2x10^6 using different turbulence models*

	C_L				C_D			
σ	***Exp***	***k-ε***	**RNG *k-ε***	***SST***	***Exp***	***k-ε***	**RNG *k-ε***	***SST***
1.79	0.790	0.796	0.809	0.799	0.030	0.030	0.025	0.022
1.48	0.795	0.784	0.803	0.798	0.033	0.032	0.027	0.025
1.25	0.821	0.783	0.802	0.809	0.039	0.034	0.031	0.029

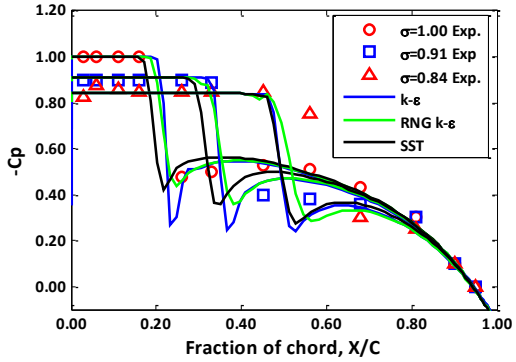

Figure 5*: Pressure distributions along the suction side of the hydrofoil, computed at AoA=4° and Re=2x10^6*

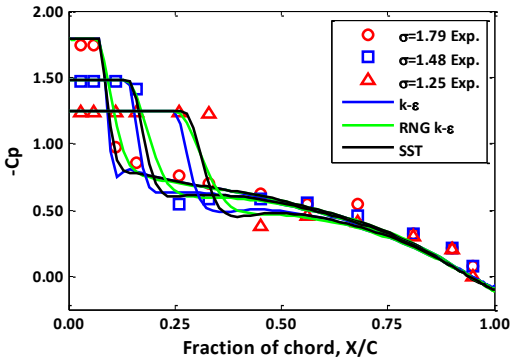

Figure 6: *Pressure distributions along the suction side of the hydrofoil, computed at AoA=6° and Re=2x10^6*

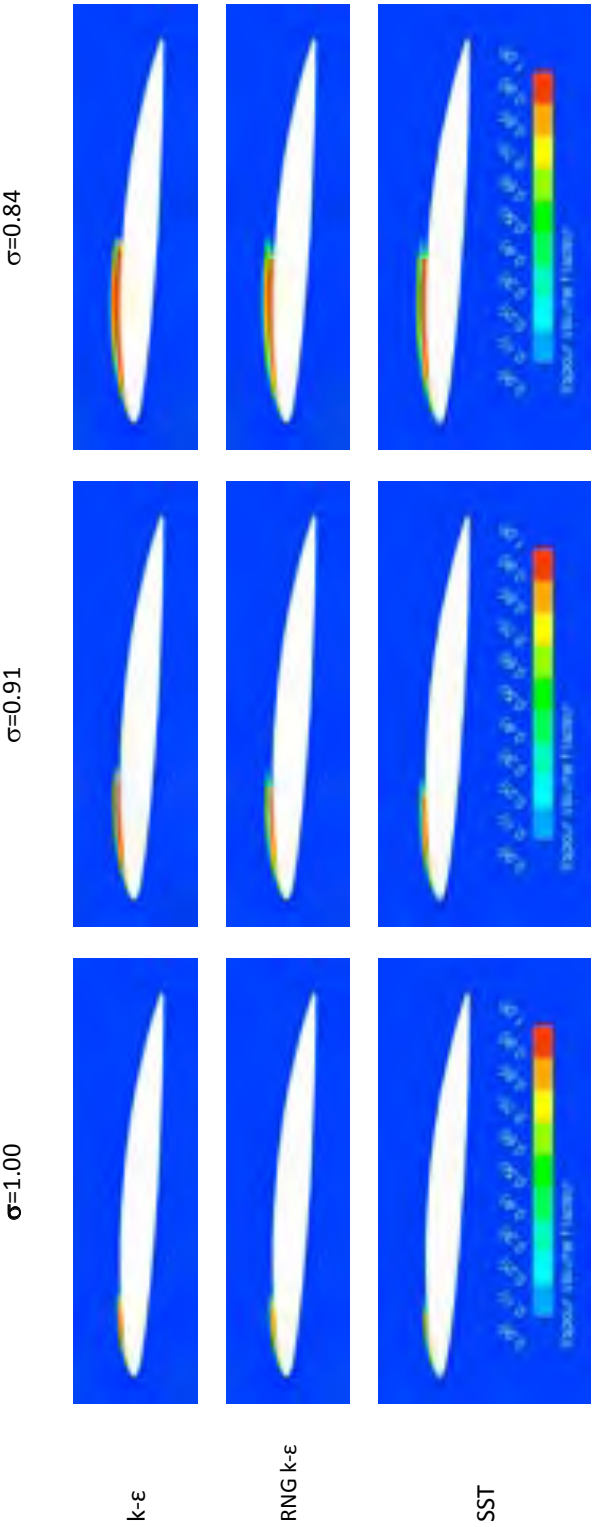

Figure 7: *Cavitation bubbles over the NACA66(MOD) hydrofoil obtained using different turbulence models. Simulations were carried out at AoA=4° and Re=2x10^6*

---

7 CONCLUDING REMARKS

Modern CFD (Computational Fluid Dynamics) technologies, which allow predicting the global characteristics and also provide detailed descriptions of the flow field of a given system/device, are nowadays routinely used during the design process. However, the accuracy of the numerical predictions can be affected by several factors. In this paper, we have investigated the influence of the turbulence model on the numerical predictions of the cavitating flow around a hydrofoil. The study was carried out with the ANSYS–CFX 12.1 commercial CFD solver. Three different turbulence models were used to simulate the cavitating flow around the NACA66(MOD) hydrofoil. More precisely we used the *k*-ε, RNG *k*-*ε* and SST turbulence models. Various cavitating flow regimes corresponding to the two different angles of incidence were considered using the previously calibrated *full cavitation model*. The numerical results shown that for the prediction of the stable sheet cavity flow over the hydrofoil only slight differences can be observed in the results obtained using the different two-equation turbulence models considered in this study.

AKNOWLEDGEMENTS

This work was performed in the context of the project OpenSHIP, Simulazioni di fluidodinamica computazionale (CFD) di alta qualità per le previsioni di prestazioni idrodinamiche del sistema carena elica in ambiente OpenSOURCE, supported by Regione FVG – POR FESR 2007-2013 Obiettivo competitività regionale e occupazione.

References

[1] **Young, F.R.,** 1999. *Cavitation*. Imperial College Press, London.

[2] **Knapp, R.T., Daily, J.W., Hammitt, F.G.**, 1970. *Cavitation*. McGraw-Hill Book Company, London.

[3] **Bouziad, Y. A.** (2006). *Physical Modelling of Leading Edge Cavitation: Computational Methodologies and Application to Hydraulic Machinery*. Ph.D. Thesis, École Polytechnique Fédérale de Lausanne, Lausanne, Switzerland.

[4] **Versteeg, H.K., Malalasekera, W.**, 2007. *An Introduction to Computational Fluid Dynamics, The Finite Volume Method.* Pearson Education Limited, Harlow, England.

[5] **Wilcox, D.C.**, *Turbulence Modeling for CFD, D C W Industries*; 2nd edition (December 2000).

[6] **Singhal, A.K., Athavale, M.M., Li, H., Jiang, Y.**, 2002. *Mathematical basis and validation of the full cavitation model.* Journal of Fluids Engineering 124 (3), 617–624

[7] **Huuva, T.**, 2008. *Large Eddy Simulation of Cavitating and Non-cavitating Flow*. Ph.D. thesis, Department of Shipping and Marine Technology, Chalmers University of Technology, Gothenburg, Sweden.

[8] **Morgut, M., Nobile E., Biluš I.**, 2010. *Comparison of mass transfer models for the numerical prediction of sheet cavitation around a hydrofoil*. Int. Journal of Multiphase Flow.

[9] **Shen, Y.T., Dimotakis, P.E.**, 1989. *The influence of surface cavitation on hydrodynamic forces.* In: Proc. 22nd ATTC, St. Johns, Canada, pp. 44–53.

JET Volume 4 (2011), p.p. 31 - 46

Issue 2, May 2011

http://www.fe.uni-mb.si/si/jet.html

USE OF AN INDUCTION MACHINE FOR THE GENERATOR OPERATING MODE IN A SMALL HYDRO POWER PLANT

UPORABA ASINHRONSKEGA MOTORJA ZA GENERATORSKO OBRATOVANJE V MALI HIDROELEKTRARNI

Matic Blaznik[ℜ], Miralem Hadžiselimović[1,2], Bojan Štumberger[1,2], Ivan Zagradišnik[1]

Keywords: induction motor, induction generator, small hydro power

Abstract

Rising demands for energy and the closure of nuclear power plants in many countries has rapidly increased the importance of harvesting energy from unconventional power sources. Small hydro power represents one of the cleanest and most frequently used renewable sources of power all over the world. Renewable energy is connected with reducing emissions and costs; therefore, the use of small rivers and streams plays a major role. Because of the many advantages that an induction machine provides, the use of an induction motor as a generator is the most suitable solution for small hydro applications. The aim of this paper is to present a practical approach for the use of an induction motor as a generator. Moreover, the operating modes of an induction machine are explained and supported with experimental measurements and calculations with the emLook motor design software.

Povzetek

Vse večje potrebe po energiji ter ukinjanje atomskih elektrarn v nekaterih državah, kaže na vse večji pomen pridobivanja električne energije iz nekonvencionalnih virov energije. Vodna energija predstavlja enega izmed najčistejših ter hkrati najpogosteje uporabljenih obnovljivih virov na svetu. Pridobivanje električne energije je velikokrat tesno povezano z zmanjšanjem

ℜ Corresponding author: Matic Blaznik, B.Sc., University of Maribor, Faculty of Electrical Engineering and Computer Science, E-mail address: matic.blaznik@uni-mb.si

[1] Faculty of Electrical Engineering and Computer Science, University of Maribor, Slovenia

[2] Faculty of Energy Technology, University of Maribor, Slovenia

---

okolju škodljivih emisij in znižanjem stroškov, zato je izkoriščanje majhnih rek in vodotokov vse bolj pomembno. Zaradi številnih prednosti je uporaba asinhronskega motorja kot generator v mali hidroelektrarni ena izmed najprimernejših rešitev. V nadaljevanju je prikazan praktičen pristop k uporabi asinhronskega stroja za generatorsko obratovanje v mali hidroelektrarni, ter določitev nazivnih vrednosti generatorja na podlagi eksperimentalnih meritev in izračunom s programskim paketom emLook.

1 INTRODUCTION

In recent decades, hydro power has gained the reputation as the most reliable and pure source of renewable energy. In 2008, hydro power supplied 15% of global electricity production. By the end of 2009, global hydro power capacity reached nearly 980 GW, including 60 GW from small hydro power, which is the second largest renewable energy source behind wind power, [1]. Increasing demands on the power supply, low start-up costs and great remunerative opportunities have been reasons for numerous investments in small hydro power plants in recent years. Although the term of "small hydro" has yet not been officially defined in terms of power, an upper limit of 10 MW (in Canada and USA up to 30 MW) is most commonly used. Furthermore, three additional sublevels are widely accepted: mini-hydro (bellow 2 MW), micro-hydro (bellow 500 kW) and pico-hydro (bellow 10 kW). In most cases these are small-scale hydro plants built as "run-of-the-river" applications, meaning that no large dam is necessary. As a result, the natural water flow is preserved and there is no negative environmental impact.

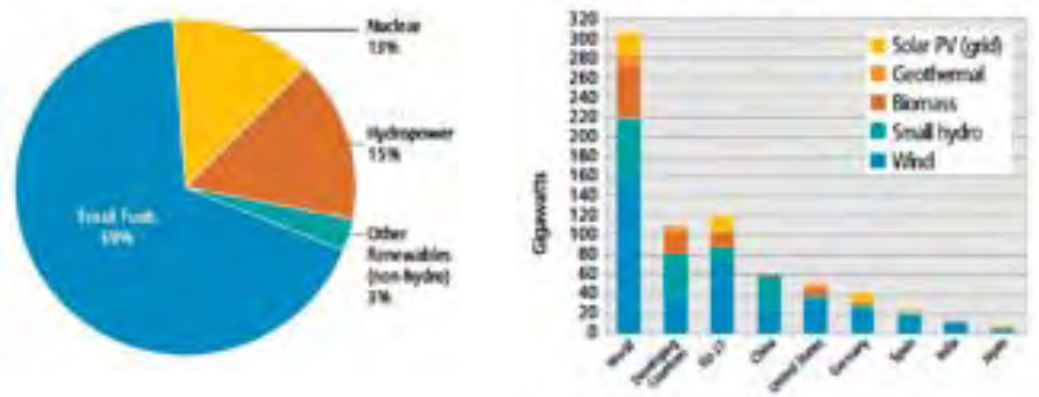

Figure 1: *Share of global electricity from renewable energy, 2008, [1] (left), Renewable power capacities in developing world, EU and top six countries, 2009, [1] (right)*

To convert the kinetic and potential energy of the stream into electrical energy, an electromechanical setup must be provided. First, hydro power must be converted into rotary mechanical power, which is done with a hydro turbine. Second, in some cases either torque or angle velocity must be adjusted through a transmission system. Finally, to perform the conversion from rotary mechanical to electrical power, a suitable generator is required. An extra control unit may necessary, depending on type of the generator. In principle, a direct current machine, a synchronous machine or an induction machine could be used as a generator. However, the most suitable generator for a small scale application (i.e. a small hydro plant) is an induction machine. The advantages of using an induction generator are: robustness, variable rotor speed ability, low maintenance costs, availability, reactive power control ability and the

fact that it requires neither a control nor a synchronization unit. Therefore, the use of an induction motor would provide an even more cost-effective solution for a small hydro plant. However, the reactive component of power is necessary to turn an induction motor into a generator; therefore, only an active component of power can be generated.

Choosing the most suitable induction motor for use as a generator in a small hydro power plant depends first of all on the type of hydro turbine and its power output range. From the standpoint of efficiency, whether a transmission system is necessary or an induction machine with greater number of poles can be used (because increasing the number of poles leads to lower efficiency) must be considered. Moreover, it is a well-known fact that the breakdown torque value of an induction machine in motor and generator operation modes is not the same. For this reason, the nominal values provided by the manufacturer must be recalculated for generator mode. This paper provides an example of determining the nominal values of an induction generator on the basis of comparison between calculation methods and experimental measurements.

2 HYDRO-MECHANICAL DRIVE SYSTEM

Knowing the rotary mechanical power produced by the shaft of hydro turbine is the basis of every single generator design, regardless of the hydro power plant size. A hydro turbine converts hydro pressure caused by the gravity and motion of water particles into rotary mechanical power, which can be expressed as,

$$P_m = \rho g Q H \eta \tag{2.1}$$

where ρ is the density of the water, g is acceleration due to gravity, Q is discharge rate, H is the net head between upper and lower water level and η is efficiency of the turbine.

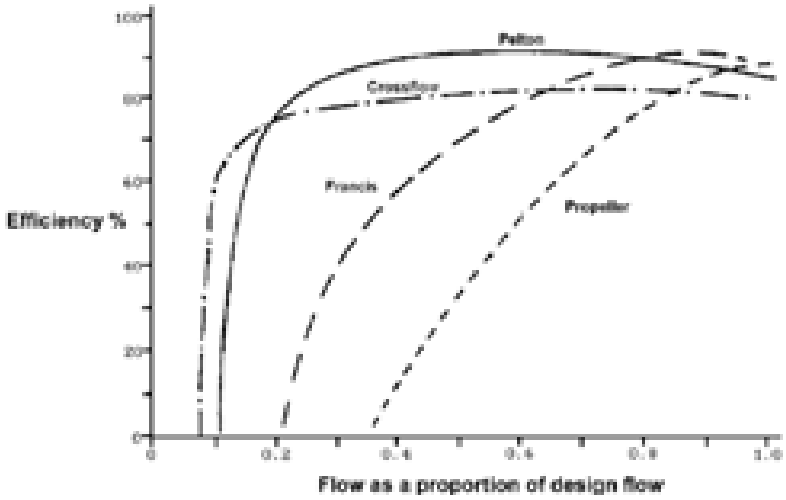

Figure 2: *Efficiencies of different hydro turbine types, [2]*

As indicated in Equation (2.1), the turbine output power not only depends on the characteristics of the water path, but also on the type of hydro turbine. There are three main types of turbines

---

that are used in small scale hydro applications: the Pelton, the Francis and the Crossflow. Each turbine has its own efficiency characteristic, which are presented in Figure 2.

As well as knowing the rotary mechanical power, is also important to know the torque-speed characteristic of the hydro turbine. Its nominal operation point is given by a shaft speed and corresponding torque, which is the basis for choosing a number of poles for an induction generator. At this point, it should be considered whether an additional transmission system is necessary to either multiply or reduce the shaft speed. However, most small-scale hydro applications are run-of-the-river types using an impulse turbine. This means that once they reach a stable operating point, the water discharge rate and pressure are constant. Therefore, a torque-speed characteristic can be provided, using a linear interdependence [3]:

$$M = M_0 - \mathrm{k}\omega \tag{2.2}$$

where M is the provided torque by hydro turbine, M_0 is the torque at zero speed, k is the slope constant and ω is shaft angle speed. Figure 3 represents the torque and output power of the turbine as a function of speed. Considering (2.2), the maximum output power $P_{\mathrm{m,max}}$ can be expressed as:

$$P_{\mathrm{m,max}} = \frac{M_0^2}{4\mathrm{k}} \tag{2.3}$$

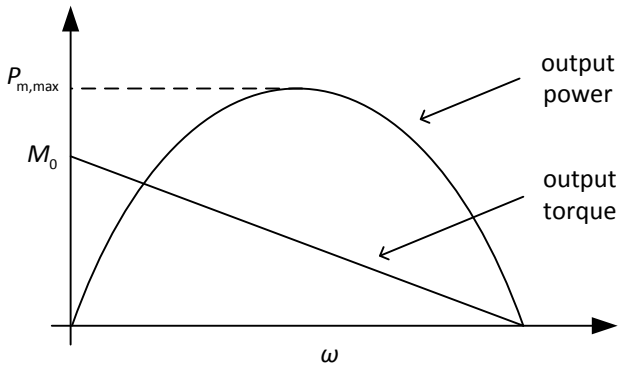

Figure 3: *Output power and torque characteristic of an impulse hydro turbine*

3 INDUCTION MACHINE OPERATING AS A GENERATOR

Basically, every induction motor is able to operate as a generator and vice versa; therefore, it is more appropriate to use the term *induction machine*. In fact, for some types of induction motors, such as a pole-changing motor, it is natural to slip into generator operation mode while switching on the winding with a greater number of poles. In other words, before the switching of the winding with lower number of poles, the machine would have speed n_1.

The other winding has a nominal speed value n_2, because of a greater number of poles, which means $n_1 > n_2$. At the moment of switching from lower number of poles to higher number of poles, the induction motor becomes an induction generator. The rotational speed of the induction motor can be expressed as

$$n = (1 - s)\frac{f}{p} \cdot 60 \tag{3.1}$$

where n is rotor speed, s is slip or the ratio between actual and relative speed, f is power supply frequency and p is number of poles, [4]. In regard to the direction of the rotating magnetic field, three operation modes are available, presented in Figure 4.

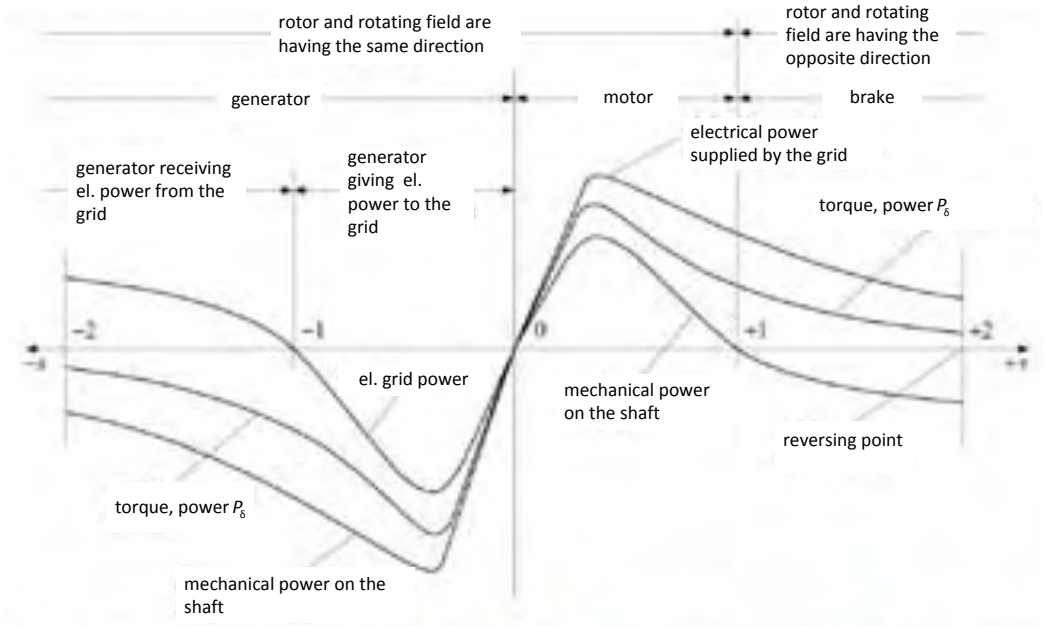

Figure 4: *Power and torque characteristics in slip area 2 ≤ s ≤ 2*

3.1 Operation modes of an induction machine

The primary difference between a generator and a motor is that a motor converts electrical energy into mechanical energy, while a generator turns mechanical energy into electrical energy. In other words, changing the operating point from a motor to a generator means that the direction of the energy flow must be changed. To achieve such an operation, the phase shift between the voltage and corresponding current must be provided. Physically, the induction machine needs reactive power to excite the main field; therefore, only active power can be generated by the induction generator. The reactive power can be supplied either out of the electrical grid or, in the case of autonomous operation, by the external source (active or passive self-excitation).

The operating modes of an induction machine and the corresponding voltage and current phasors can be represented with a circle diagram of an induction machine, developed by Johann Ossanna in 1894, [5]. The circle diagram shows the changing size and phase angle of stator current phasor for every value of slip. In other words, it represents the $\underline{I}_s = f(s)$ curve. The fundamental circle diagram can be derived on the basis of simplified equivalent circuit of an induction motor (Figure 5) and its voltage equations, [4]:

$$\begin{aligned}\underline{U}_s &= -\left(R_s + \mathrm{j}X_{\sigma s}\right)\underline{I}'_r + \mathrm{j}X_m\left(\underline{I}_s + \underline{I}'_r\right)\\ 0 &= \left(\frac{R'_r}{s} + \mathrm{j}X'_{\sigma r}\right)\underline{I}'_r + \mathrm{j}X_m\left(\underline{I}_s + \underline{I}'_r\right)\end{aligned} \tag{3.2}$$

where $\underline{U}_s$ is stator voltage, $\underline{I}_s$ is stator current, R_s is stator resistance, $X_{\sigma s}$ is stator leakage reactance, $\underline{I}'_r$ is rotor current transformed to the stator, R'/s is rotor resistance transformed to the stator, $X'_{\sigma r}$ is rotor leakage reactance transformed to the stator, X_m is magnetizing reactance and $\underline{I}_m$ is magnetizing component of current.

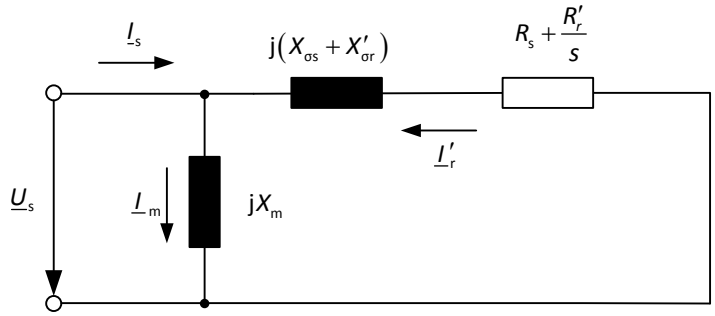

Figure 5: *Simplified equivalent circuit of an induction machine*

Considering the graphic procedure of inversion of complex values, the track of $\underline{I}_s$ can be provided and its characteristic values at $s = 0,\ 1$ and $\pm\infty$. The track of stator current is represented in Figure 6 as a circle diagram.

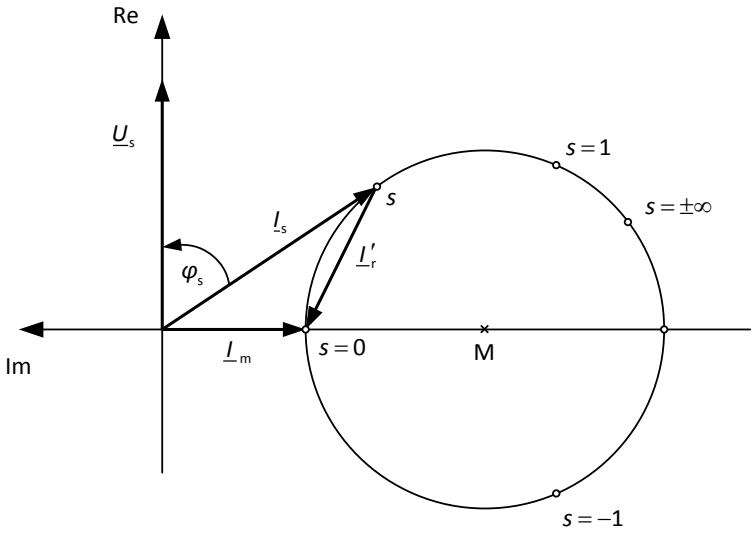

Figure 6: *Basic circle diagram of an induction machine*

The circle diagram presented in Figure 6 is basic, because it does not take into account energy losses in the iron core. To consider such losses, the watt component of current $\underline{I}_w$ must be

added to the magnetizing current $\underline{I}_m$. Consequentially, the centre point of the circle rises above the imaginary axis, as shown in Figure 7.

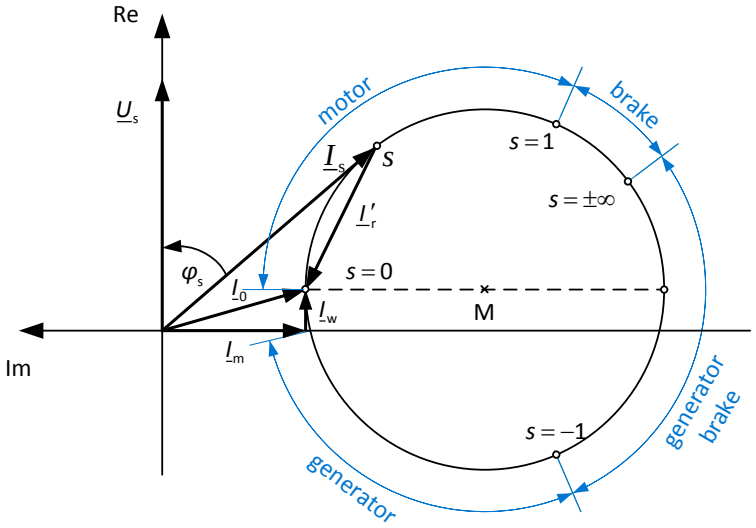

Figure 7: *Circle diagram considering the watt component of the current*

Moreover, power and torque characteristics can be obtained from the circle diagram by constructing corresponding lines of slip, power and torque. Because the circle diagram is situated above the imaginary axis, its absolute value of the stator current in the motor area and generator area at the same speed is different. For this reason, the current and torque characteristic in motor operation mode is not the same as in the generator operation mode. The breakdown torque value in the generator area can be up to five times greater as in the motor area. A practical difference is presented in Figure 8, considering two motors with different number of poles.

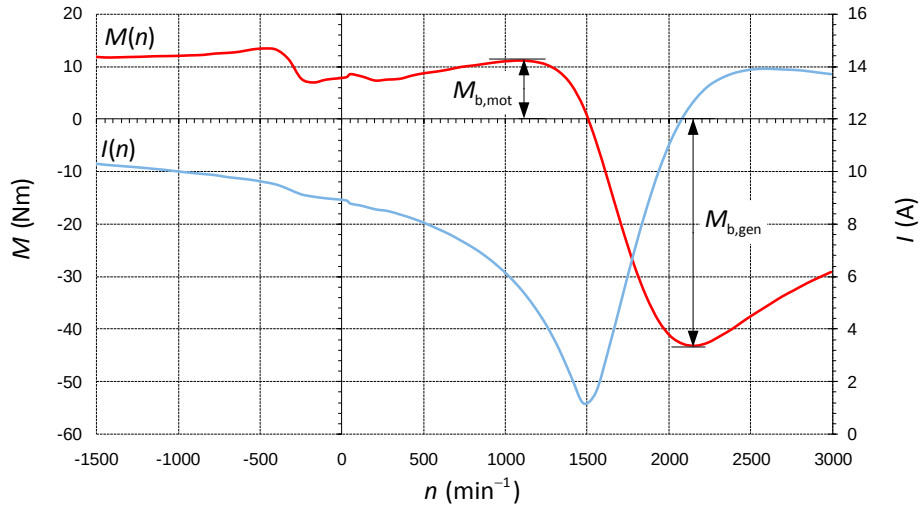

a)

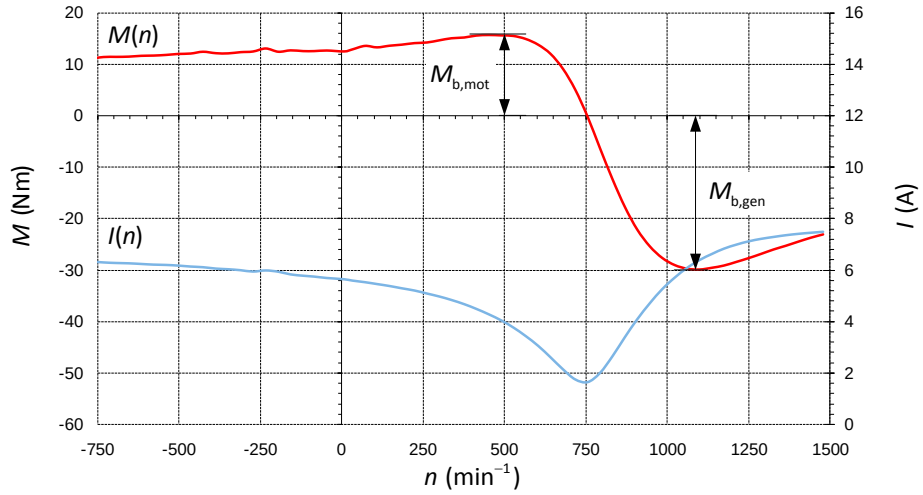

b)

Figure 8: *Torque and current characteristics of an induction machine for a) 8 poles and b) 4 poles*

3.2 Conversion of energy

To determine the nominal power value of the induction generator, on the basis of its motor nominal values, it is important to know the flow of energy in each operation mode.

In the case of a motor, the electrical grid represents the source of power. Electrical power is provided to the stator P_s, which covers the winding losses of the stator P_{Cus} and iron core losses P_{Fe} of the stator. The rest of the power is supplied through the energy gap to the rotor P_δ, where it is being used to cover the winding losses of the rotor P_{Cur} and the losses of friction and ventilation P_{frv}. The rest of the power is provided to the rotor P_r, which is in nominal conditions known as nominal power P_r. The corresponding flow of power is presented in Figure 9a.

$$\begin{aligned} P_s &= P_{Cus} + P_{Fe} + P_\delta \\ P_\delta &= P_{Cur} + P_{frv} + P_r \end{aligned} \tag{3.3}$$

The efficiency of motor energy conversion is defined as:

$$\eta = \frac{P_r}{P_s} \tag{3.4}$$

The same energy losses must be covered in the case of a generator. The difference is that the source of power is mechanical power provided to the shaft of the generator P_r and the output power is from the stator provided to the grid P_s. Additionally, reactive power is necessary to establish the main magnetic flux and leakage flux of the stator and rotor. Therefore, an external source of reactive power must be provided, because only active power can be provided through the shaft of generator.

$$P_r = P_{Cur} + P_{frv} + P_\delta$$
$$P_\delta = P_{Cus} + P_{Fe} + P_s \tag{3.5}$$

The efficiency of generator energy conversion is defined as:

$$\eta = \frac{P_s}{P_r} \tag{3.6}$$

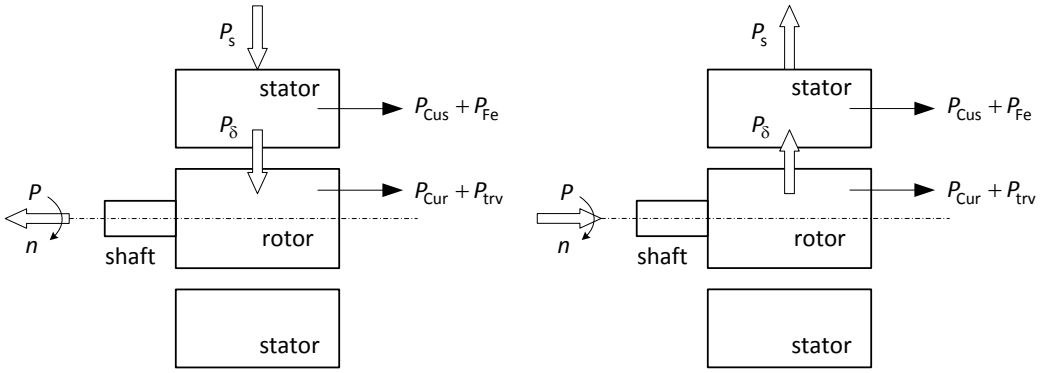

Figure 9: *Sankey chart of power flow for a) motor and b) generator*

4 EXPERIMENTAL MEASUREMENTS

The nominal point of the induction generator was determined by performing a load test of the induction machine. Once the possible nominal point of the induction generator had been chosen, the temperature rise test was performed to confirm the permanent operation of the induction generator at chosen nominal conditions. For this reason, the experimental setup was established to perform load tests of the induction machine and temperature measurements. In addition to experimental measurements, the calculations of parameters and values were made using the emLook motor design program, [6].

4.1 Experimental setup

A tested motor was coupled to the regulated drive system, which served either as a mechanical load or an external source of mechanical power. Stator windings were connected to the grid through a suitable autotransformer. The electrical values were measured using a *Norma D 6100 M* power analyser. The value of temperature was measured at several points of the tested motor using type J thermo elements in combination with a *NI Fieldpoint FP-120 data acquisition device*.

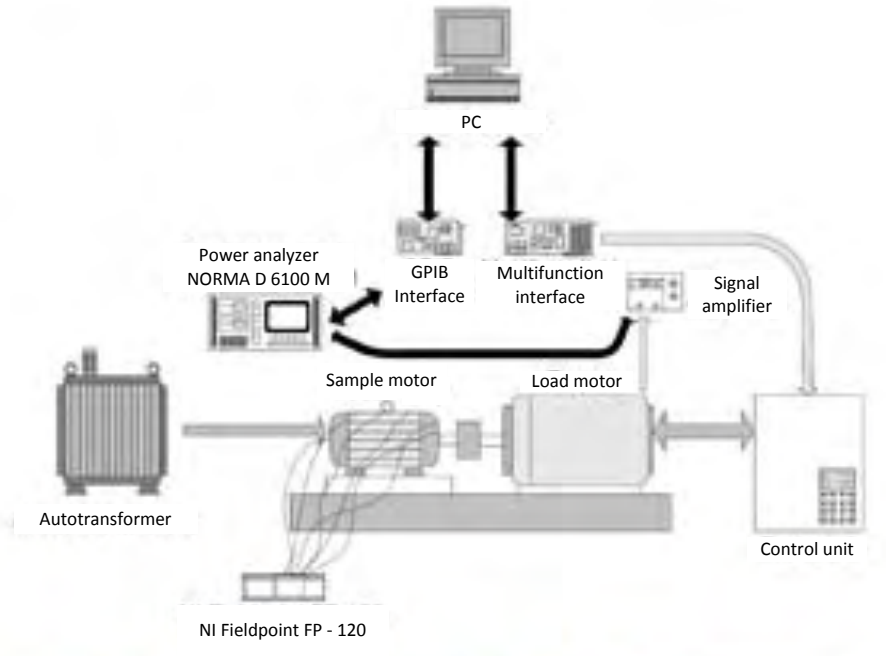

Figure 10: *Experimental measurement system setup*

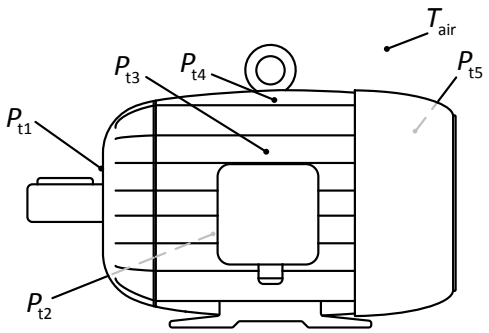

Figure 11: *Temperature measuring points on induction machine*

4.2 Presentation of tested induction machine

As a test machine, an air-cooled induction motor with an aluminium squirrel cage rotor was used. The shaft height was 132 mm and the length of the stator package was 180 mm. The motor had 36 slots on the stator and 28 slots on the rotor. The conductive bars of the squirrel cage were shifted by one rotor slot. The nominal data of the tested induction motor are presented in Table 1.

Table 1: *Nominal data of the tested induction motor*

Type	2M 132 M4
Nominal voltage U_N	Y400 V
Nominal current I_N	15,8 A
Nominal power P_N	7,5 kW
Power factor *PF*	0,80
Number of poles	2*p*=2
Nominal frequency f_N	50 Hz
Nominal speed n_N	1450 min^{-1}
Nominal torque M_N	49,4 Nm
Starting torque to nominal torque ratio M_s/M_N	2,5
Breakdown torque to nominal torque ratio M_b/M_N	3,0
Starting current to nominal current ratio I_s/I_N	7,0
Isolation class	F
IP protection level	54

The tested motor had a three-phase winding on the stator, which is presented as a wiring diagram in Figure 12. The type of used winding was a double layer lap winding, shortened for two stator slots with a coil pitch of 1 – 8.

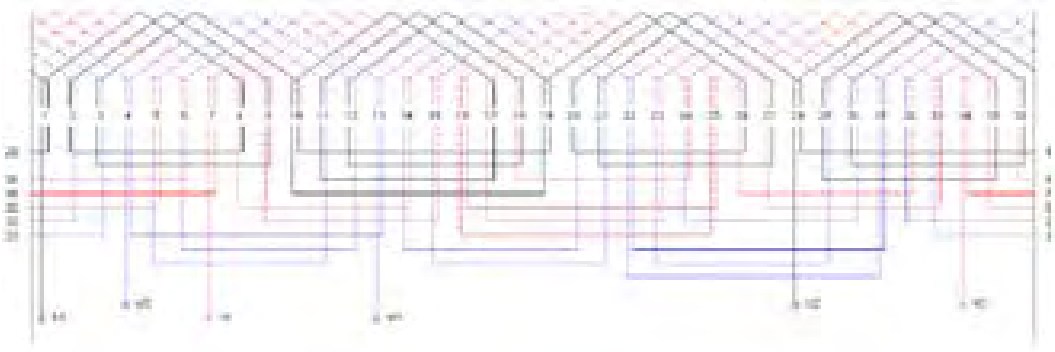

Figure 12: *Layout of the three-phase winding used in the tested machine*

4.3 Load test of induction machine

First, the load motor test provides the nominal values of the induction machine in the motor operation area. Furthermore, the load generator test provides the expected nominal values of the generator operation mode. The results of load motor test and load generator test are

---

presented in Figures 13 and 14. The nominal values have been determined on the basis of the load motor test and the load generator test, which are presented in Table 2 (motor operation area) and in Table 3 (generator operation area).

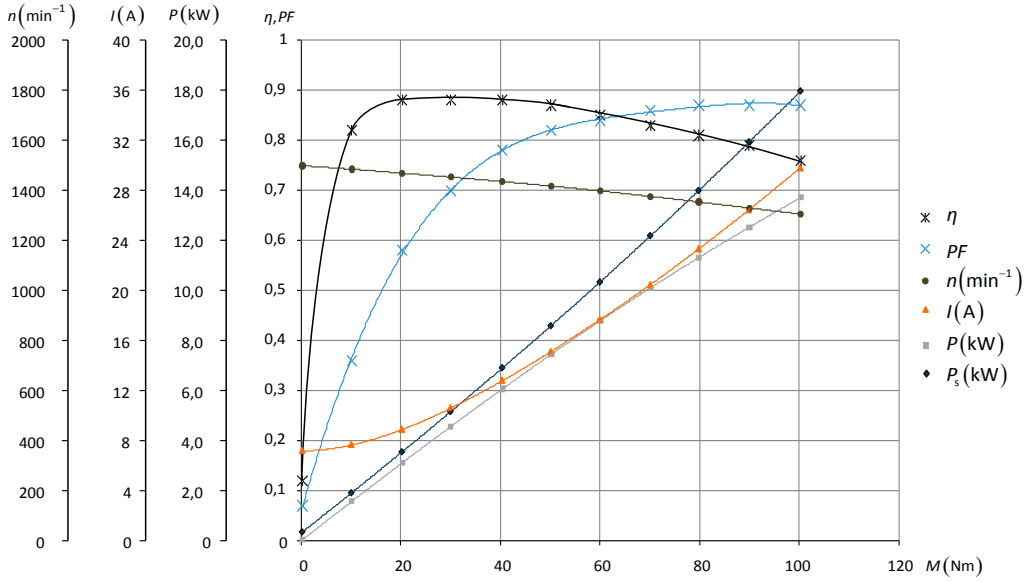

Figure 13: *Load motor test of the tested induction machine*

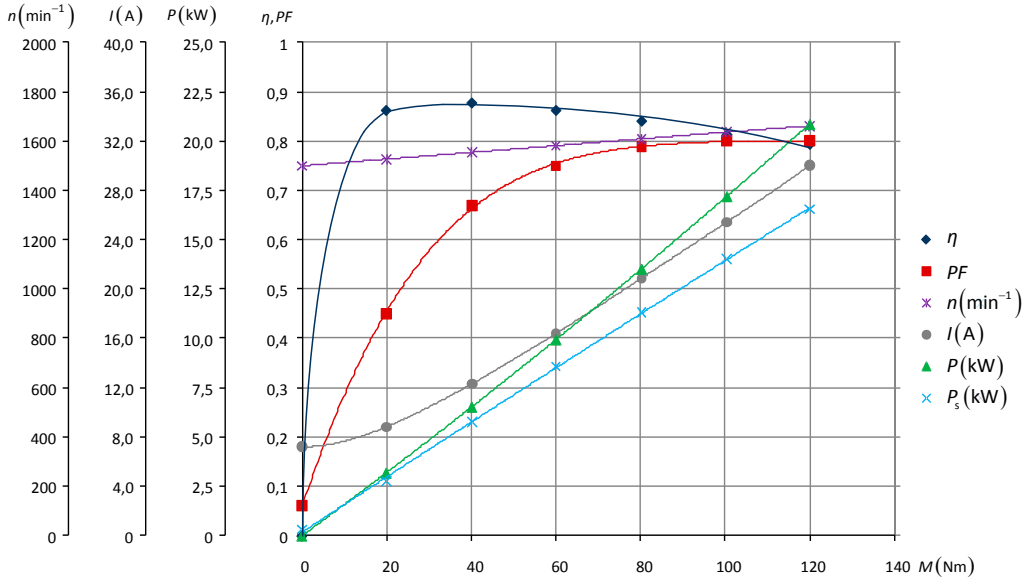

Figure 14: *Load generator test of the tested induction machine*

On the basis of the provided load tests of the induction motor and generator, the nominal point of the generator was chosen at produced power P = 8 kW. The measurement results, in comparison to the emLook calculations, are proved in Table 2 (motor operation mode) and in Table 3 (generator operation mode).

Table 2: *Measured and calculated nominal values of motor operation mode*

	I (A)	P_s (W)	P_r (W)	PF	η	n (min^{-1})
emLook	15,21	8716,7	7500,0	0,827	0,860	1439
measurement	15,22	8622,0	7500,0	0,822	0,866	1417

Table 3: *Measured and calculated nominal values of generator operation mode*

	I (A)	P_s (W)	P_r (W)	PF	H	n (min^{-1})
emLook	14,89	8935,0	8001,2	0,776	0,895	1553
measurement	15,54	9235,0	8000,0	0,743	0,880	1576

4.4 Temperature rise test

Further determinations of the nominal values for the generator operation mode were obtained with temperature rise tests, to assure that the generator can permanently operate at the chosen nominal values. Temperature rise tests were performed through the measurement of the temperature at several points on the machine housing and by measuring the winding resistance. Immediately after the temperature measurement, the winding resistance was measured, providing the curve of resistance fall while the machine is cooling down. On the basis of already measured resistances at room temperature, the extrapolation of the measured curve can be performed, which provides the temperature of the winding ϑ_s at the moment of the end of the test.

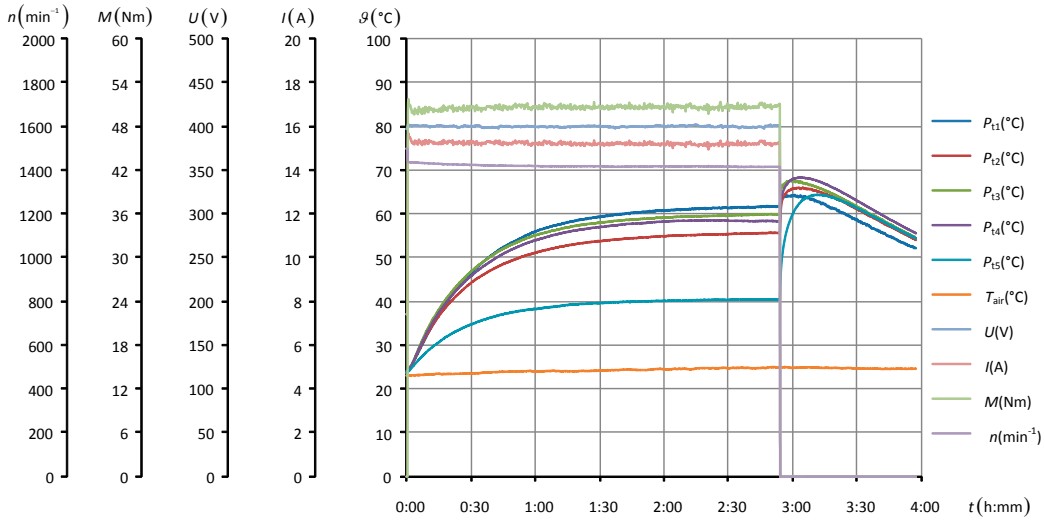

Figure 15: *Temperature rise test of the induction machine operating as a motor*

First, the heating test of the induction machine in motor operation mode was performed (Figure 15) to discover the losses at nominal operating values (P = 7,5 kW). Second, the heating test of

---

the machine in generator operating mode (Figure 16), was carried out to precisely determine the electro-mechanical nominal values.

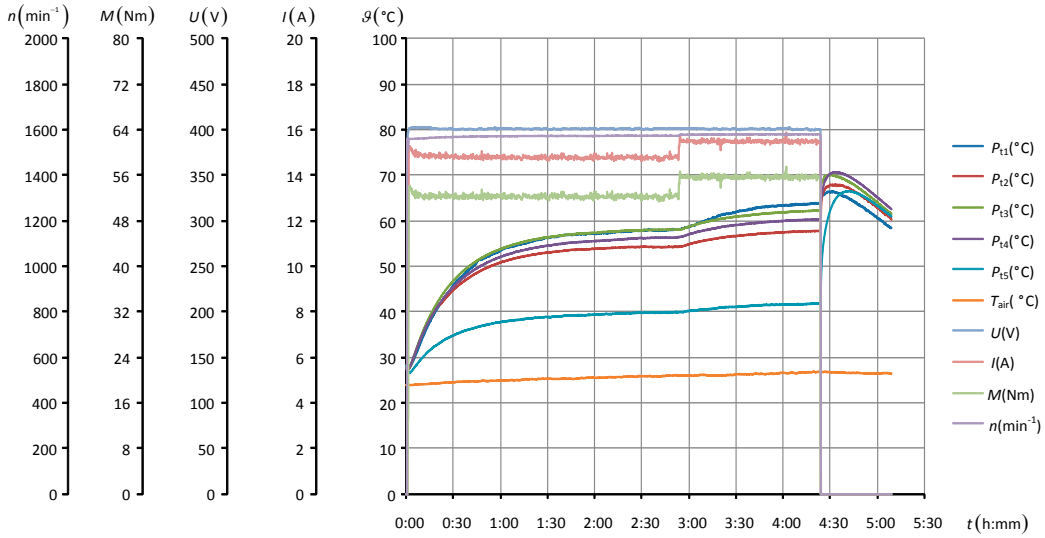

Figure 16: *Temperature rise test of the induction machine operating as a generator*

The measurements results are provided as a comparison of over temperatures between motor and generator operating modes (Table 4). Additionally, the comparison of electro-mechanical values is presented in Table 5.

Table 4: *Comparison of measured over temperatures of motor and generator*

	P (kW)	P_{t1} (K)	P_{t2} (K)	P_{t3} (K)	P_{t4} (K)	P_{t5} (K)	$\Delta\vartheta_s$ (K)
Motor	7,5	36,82	30,68	34,83	33,25	15,43	68,43
Generator	8,0	36,99	30,87	35,25	33,47	14,99	68,49

Table 5: *Comparison of nominal electro-mechanical values for both operating modes*

	P (kW)	I (A)	P_s (kW)	Q (kVar)	S (kVA)	n (min^{-1})	PF	η	s (%)	P_{loss} (W)
Mot.	7,50	15,24	8,667	6,116	10,609	1417	0,82	0,87	5,45	1167
Gen.	9,17	15,54	8,000	-7,118	10,710	1575	0,75	0,88	-5,07	1166

The comparison of electro-mechanical values is relevant, because the tested induction machine was connected to the electrical grid during the measurements of both operating modes. Therefore, the voltage and frequency were continuously constant (U = 400 V, f = 50 Hz).

Table 6: *Nominal data of the tested induction machine in generator mode*

Type	2M 132 M4
Nominal voltage U_N	Y400 V
Nominal current I_N	15,54 A
Nominal power P_N	8,0 kW
Reactive power Q_N	7,118 kVAr
Power factor *PF*	0,75
Number of poles	2*p*=2
Nominal frequency f_N	50 Hz
Nominal speed n_N	1575 min^{-1}
Nominal torque M_N	55,54 Nm
Isolation class	F
IP protection level	54

5 CONCLUSIONS

The comparison of experimental measurements has shown that use of an induction motor as a generator not only provides a simple solution, but also an energy efficient way of using an induction machine in a small hydro power plant.

The measurement results have proved that the output power of the induction generator is greater than the output power of the same induction machine, when operating as an induction motor, considering the same value of the nominal stator current. In our case, the difference between motor output power and generator output power was approximately 6%. Moreover, on the basis of motor nominal values, the generator nominal values were determined (Table 6), which are necessary data for a small hydro power plant design.

Additionally, the choice of an induction motor could be optimized by using an induction motor with better efficiency, which could be obtained through using semi-finished sheet metal, more suitable winding for a generator operating mode or a better cooling system. Furthermore, the power factor could be improved by using supplementary capacitors.

References

[1] **Renewable Energy Policy Network for the 21st Century:** *Renewables 2010 Global Status Report,* REN21 Secretariat, pp. 16–21, 2011

[2] **O. Paish:** *Small hydro power: Technology and current status,* Elsevier Science, Renewable and Sustainable Energy Reviews, Volume 6, Issue 6, pp. 537–556, 2002

---

[3] **J. S. Gulliver, R. E. A. Arndt:** *Hydropower Engineering Handbook*, McGraw-Hill, pp. 440–443, 1991

[4] **I. Zagradišnik, B. Slemnik:** *Električni rotacijski stroji,* Fakulteta za elektrotehniko, računalništvo in informatiko Maribor, Volume 5, pp. 77–125, 2009

[5] **T. Fladerer:** *Der Asynchrongenerator im Kleinkraftwerk,* Loher GmbH Ruhstorf, 2004

[6] **I. Zagradišnik, M. Hadžiselimović, J. Ritonja, B. Slemnik:** *The emLook Software Package for the Analytical and Numerical Analysis of Electrical Machines,* Przegląd Elektroniczny, Volume 12, pp. 175–178, 2010

[7] **S. S. Murthy, B.P. Singh, C. Nagamani, K.V.V. Satyanarayana:** *Studies on the Use of Conventional Induction Motors as Self-Excited Generators,* IEEE Transactions on Energy conversions, Volume 3, No. 4, pp. 842–848, 1988

[8] **R. C. Bansal:** *Three-Phase Self-Excited Induction Generators: An Overview,* IEEE Transactions on energy conversion, Volume 20, No. 2, pp. 292–299, 2005

[9] **C. Dragu, T. Sels, R. Belmans:** *Small Hydro Power – State of the Art Applications,* ESAT/ELECTA, KU Leuven, 2009

Nomenclature

Symbol	Meaning
P	Active power
S	Apparent power
Q	Reactive power, water discharge rate
H	Net head between upper and lower water
M	Torque
ω	Angle speed
n	Shaft speed
s	Slip
f	Frequency
p	Number of poles
U	Voltage
I	Current
R	Resistance
X	Reactance
η	Efficiency

JET Volume 4 (2011), p.p. 47–54

Issue 2, May 2011

http://www.fe.uni-mb.si/si/jet.html

WATER HAMMER CAUSED BY SHUT-OFF VALVES IN HYDROPOWER PLANTS

VODNI UDAR POVZROČEN Z ZAPIRALI V HIDROELEKTRARNAH

Uroš Karadžić[ℜ], Anton Bergant[1], Petar Vukoslavčević[2], Esad Sijamhodžić[3], Drago Fabijan[4]

Keywords: water hammer, shut-off valve, hydropower plant

Abstract

This paper investigates water hammer effects caused by the closure of shut-off valves against discharge. Shut-off valves (turbine inlet valves) in hydropower plants (HPP) can be either of spherical or butterfly type. These valves are traditionally used as safety elements in the system and are closed against discharge only in emergency cases such as turbine runaway and pipeline bursts. Usually, the closure of shut-off valves is controlled by the valve actuator (hydraulic servomotor). Because the hydraulic torque that acts on the valve body is dependent on flow conditions, the valve closing time may vary significantly for different flow velocities. The closure of the shut-off valve can be modelled as passive or active. The passive valve model takes into consideration the dynamic equation of the valve body motion, and the valve closure time is a result of numerical simulation. In the active valve model, the closure time is known in advance. The results of measurements and corresponding numerical simulations for the closure of a butterfly valve from the Lomščica HPP, Slovenia and the closure of a spherical valve from the

[ℜ] Corresponding author: Uroš Karadžić, PhD, Univerzitet Crne Gore,Mašinski fakultet, Džordža Vašingtona bb, 81000 Podgorica, Montenegro, uros.karadzic@ac.me

[1] Anton Bergant, PhD, Litostroj Power d.o.o., Litostrojska 50, 1000 Ljubljana, Slovenia, anton.bergant@litostrojpower.eu

[2] Petar Vukoslavčević, PhD, Univerzitet Crne Gore,Mašinski fakultet, Džordža Vašingtona bb, 81000 Podgorica, Montenegro, petarvuk@ac.me

[3] Esad Sijamhodžić, BSc, Litostroj Power d.o.o., Litostrojska 50, 1000 Ljubljana, Slovenia, esad.sijamhodzic@litostrojpower.eu

[4] Drago Fabijan, PhD, Litostroj Power d.o.o., Litostrojska 50, 1000 Ljubljana, Slovenia, drago.fabijan@litostrojpower.eu

Perućica HPP, Montenegro are presented. The results for both valves are given for closure against the discharge from maximum (full-load) and half of the maximum discharge (half-load). It is shown that for the case of butterfly valve, the closing time varies significantly with respect to flow conditions. In contrast, the spherical valve closing time is practically the same regardless of hydraulic loads.

Povzetek

Prispevek obravnava vpliv vodnega udara povzročenega z manevri zapiral. Predturbinska zapirala v hidroelektrarnah so lahko kroglasti zasuni ali lopute. Ta zapirala so pogosto uporabljena kot varnostni gradniki v sistemu. Zapirajo v havarijskih režimih obratovanja kot sta pobeg turbine ali porušitev cevovoda. Zapiranje je krmiljeno z aktuatorjem (hidravlični servomotor). Ker je hidravlični moment na telo ventila odvisen od pretočnih pogojev se lahko časi zapiranja močno razlikujejo za različne pretočne hitrosti. Zapiranje lahko modeliramo kot aktivno ali kot pasivno. Pasivni model zajema dinamično enačbo gibanja telesa zapirala pri čemer je rezultat izračuna čas zapiranja. Pri aktivnem modelu je čas zapiranja v naprej določen. Prispevek obravnava rezultate meritev in izračuna za zapiranje lopute v HE Lomščica, Slovenija in rezultate za zapiranje kroglastega zasuna v HE Perućica, Črna gora. V obeh primerih so rezultati podani za zapiranje pri polnem (največjem) in pri delnem (polovičnem) pretoku. Izkaže se, da je čas zapiranja lopute močno odvisen od velikosti pretoka. Temu ni tako pri zapiranju kroglastega zasuna, kjer je čas zapiranja praktično enak pri polnem in delnem pretoku.

1 INTRODUCTION

Water hammer is the phenomenon of a pressure rise or drop in penstocks of hydropower plants and pumping stations due to a change in flow conditions. Water hammer loads must be kept within the prescribed limits, because they can disturb the operation of the hydraulic system and damage the system components. During the construction of new or the modernization of existing hydropower plants, a detailed water hammer analysis is required in order to determine the maximum and minimum permissible pressures as two of the most important parameters in the design process of the plant components. In hydropower plants, water hammer is induced by turbine load acceptance and reduction, load rejection under governor control, emergency shut-down and unwanted runaway, and the closure and opening of the safety shutoff valves. This paper investigates water hammer effects caused by the closure of shut-off valves against the discharge.

In the first part of the paper, mathematical tools for solving water hammer equations are briefly introduced. Water hammer is described with continuity and momentum equations and equations describing boundary elements (reservoir, valve, surge tank, turbine). The shut-off valve closure is modelled as *passive*, where the closing time is dependent on torques that act on the valve body.

In the second part of the paper, comparisons of calculated and measured results are made. Measurements have been performed in the Lomščica HPP, in Slovenia for the butterfly valve closure case and in the Perućica HPP, in Montenegro for the case of the spherical valve closure. Both valve closure cases have been carried out against the discharge from full and half-load

(maximum and half of the maximum discharge). It is shown that flow conditions have significant impact on butterfly valve closure time, but minor influence on spherical valve closure time.

2 THEORETICAL MODELLING

Water hammer in pipelines is fully described by the continuity equation and equation of motion [1],

$$\frac{\partial H}{\partial t}+\frac{a^2}{gA}\frac{\partial Q}{\partial x}=0\,, \tag{2.1}$$

$$\frac{\partial H}{\partial x}+\frac{1}{gA}\frac{\partial Q}{\partial t}+\frac{fQ|Q|}{2gDA^2}=0\,. \tag{2.2}$$

Note that all symbols are defined in the Nomenclature. A quasi-steady approach to estimate friction losses in the penstock is satisfactory for the slow transients considered in this paper. Equations (2.1) and (2.2) are solved by the method of characteristics (MOC) using the staggered numerical grid [2]. At a boundary (reservoir, shut-off valve, turbine), a device-specific equation is used instead one of the MOC water hammer compatibility equations.

The instantaneous discharge through the shut-off valve can be obtained from the following equation,

$$Q_{u,t}=\sqrt{\frac{K_D^2}{1-K_D^2}}A_v\sqrt{2g\left(H_{u,t}-H_{d,t}\right)}\,. \tag{2.3}$$

For the passive valve model, an additional dynamic equation of the valve body motion is needed,

$$J\frac{d^2\Theta}{dt^2}=\sum T\,. \tag{2.4}$$

A detailed derivation of this equation can be found in Bergant and Sijamhodžić [3] for the Lomščica HPP butterfly valve and in Karadžić *et al.* [4] for the Perućica HPP spherical valve.

3 DESCRIPTION OF SYSTEMS INVESTIGATED

Figure 1 shows schematic layout of the Lomščica HPP, in Slovenia, with its main parameters. It is comprised of an upstream reservoir, emergency valve, penstock, turbine shut-off valve, Francis turbine equipped with pressure regulating valve, and a tailrace. The total length of the penstock system is L = 715.5 m and the diameter is D = 1000 mm. The turbine safety valve is the butterfly type equipped with a passive actuator comprised of an external weight and hydraulic servomotor.

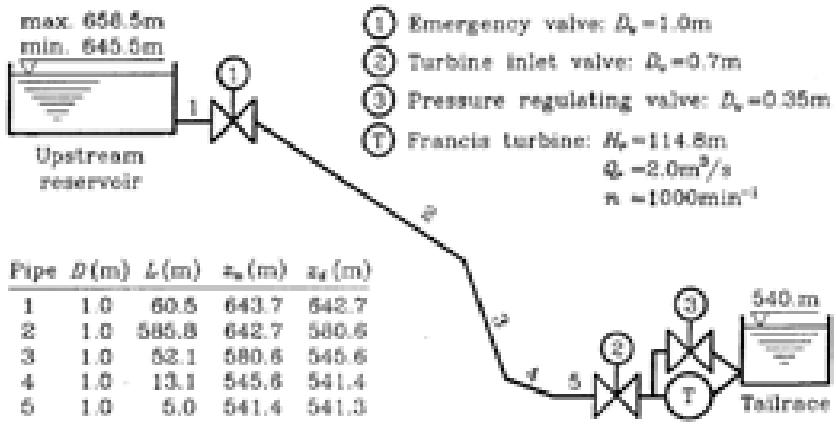

Pipe	D(m)	L(m)	z_u(m)	z_d(m)
1	1.0	60.5	643.7	642.7
2	1.0	585.8	642.7	580.6
3	1.0	52.1	580.6	545.6
4	1.0	13.1	545.6	541.4
5	1.0	5.0	541.4	541.3

Figure 1: *Layout of Lomščica HPP, Slovenia [3].*

Figure 2 shows a schematic layout of the Perućica HPP, in Montenegro. The Perućica HPP is a complex system comprised of an upstream reservoir, concrete tunnel, surge tank with expansion and overflow, three parallel steel penstocks that feed seven horizontal shaft Pelton turbine units with a gross installed capacity of 307.0 MW, and a tailrace. Two safety spherical valves are attached to each Pelton turbine unit. The valves are equipped with a passive actuator comprised of a hydraulic servomotor that is closed by pressurized water from the penstock and opened by oil pressure from the hydraulic power unit. A detailed description of the Perućica HPP flow-passage system with its main characteristics can be found in Karadžić *et al*. [5].

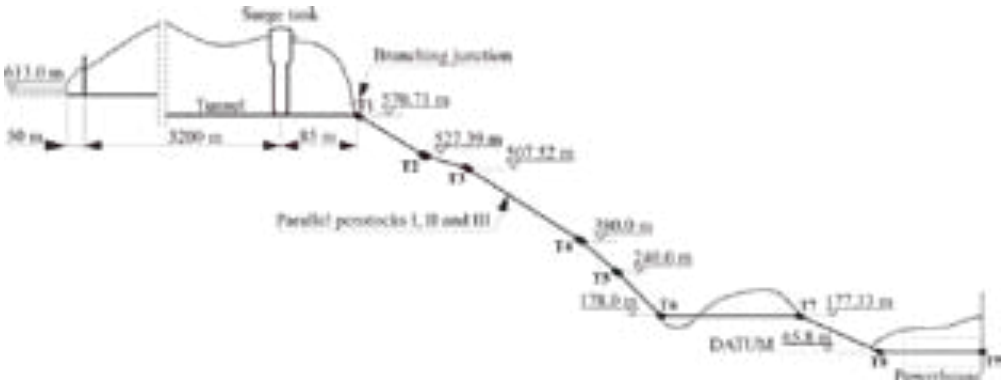

Figure 2: *Layout of Perućica HPP, Montenegro [4].*

4 COMPARISONS OF COMPUTED AND FIELD TEST RESULTS

This paper presents numerical and experimental results given for the closure of shut-off valves against the discharge. Figure 3 shows measured and calculated pressure heads (heads) at the upstream end of the butterfly valve as well as the valve openings for the cases of valve closure against the discharge from the full and half-load at the Lomščica HPP. The maximum calculated

water hammer head of H_{max} = 129.8 m at the upstream side of the valve (taken at elevation z_v = 541.3 m) at full-load operation of the plant is slightly higher than the measured head of H_{max} = 127.6 m (Fig. 3a). The calculated and measured head rises in this case are ΔH = 20.8 m and ΔH = 18.6 m, respectively. In the case of half-load plant operation the situation is also similar. The maximum calculated and measured heads are H_{max} = 127.7 m and H_{max} = 127.0 m with head rises of ΔH = 14.9 m and ΔH = 14.2 m, respectively (Fig 3c). The discrepancies in amplitude and phase shift are larger at small valve openings (complex flow structure). The maximum measured and calculated heads are less than the prescribed maximum head H_{max} = 130 m. The valve closure time is much longer for the case of half-load plant operation (t_c = 196 s, Fig. 3d) than for the case of full-load operation (t_c = 127.7 s, Fig. 3b). Flow conditions have significant influence on the valve closing time in case of butterfly valve closure against the discharge.

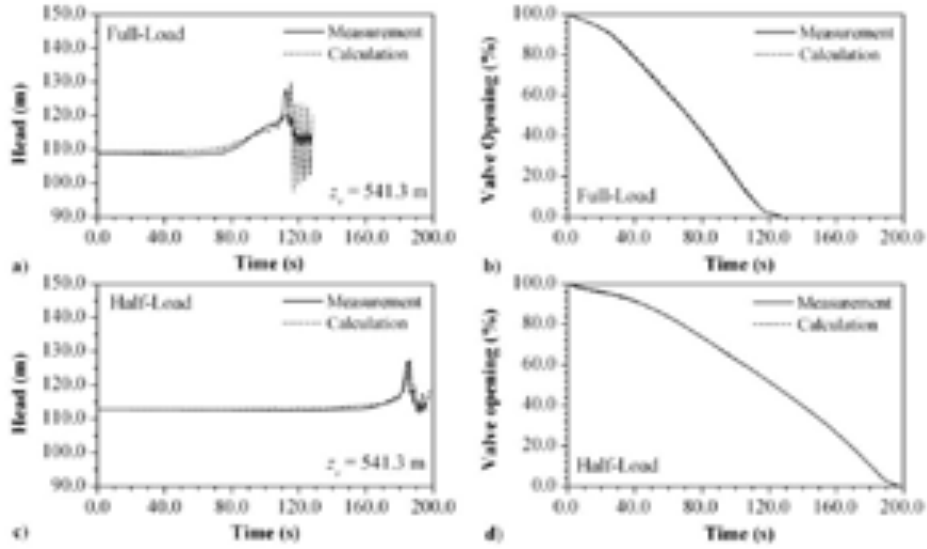

Figure 3: *Comparisons of measured and calculated heads at the upstream end of the butterfly valve and valve openings. Lomščica HPP, Slovenia.*

Numerical and measured heads at the upstream end of the spherical valve and the valve openings for the cases of valve closure against discharge from the full and half-load at the Perućica HPP are shown in Fig. 4. The maximum measured head, for the case of full-load plant operation, of H_{max} = 560.58 m (taken at elevation z_v = 65.8 m) occurred at the end of valve closing period with a head rise of ΔH = 25.8 m. The maximum calculated head is H_{max} = 561.1 m with a head rise of ΔH = 25.2 m. The numerical valve model shows good agreement with the results of measurement during the valve closing period. The maximum head occurs a few seconds prior to the complete valve closure (Fig. 4a). After the valve is fully closed, the numerical model simulates pressure trace reasonably well but with little attenuation. The calculated valve closure time is equal to the measured one of t_c = 200 s (Fig. 4b). For the case of half-load plant operation, the maximum measured head is H_{max} = 560.6 m with a head rise of ΔH = 22.1 m. The maximum numerical head value and head rise are H_{max} = 551.9 m and ΔH = 13.4 m, respectively. The numerical model shows reasonable agreement with data from measurements during and after the valve closure period (Fig. 4c). For both investigated cases, the maximum measured and calculated heads are much less than the maximum permissible system head of 602 m. The calculated valve closure time is t_c = 194 s; this is three seconds

shorter than the measured valve closure time of 197 s (Fig. 4d). It may be concluded that the hydraulic servomotor orifice is set adequately, so the valve closing time is always about 200 s regardless of the hydraulic loads on the valve body during the valve closure against the discharge or in even still water.

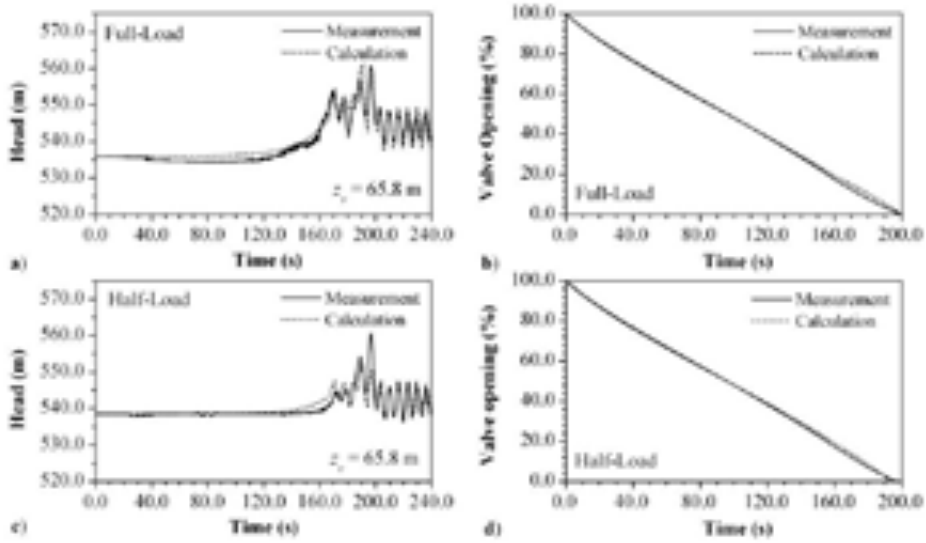

Figure 4: *Comparisons of measured and calculated heads at the upstream end of the spherical valve and valve openings. Perućica HPP, Montenegro.*

5 CONCLUSIONS

Numerical results are compared with the results of measurements given for the closure of shut-off valves against the discharge from plants at full and half-loads of operation. From the results presented, it may be concluded that for the closure of the butterfly valve (Lomščica HPP), the valve closing time is highly dependent on flow conditions, i.e. the closing time is much longer for cases at half-load. In contrast, in case of the spherical valve closure (Perućica HPP), the valve closing time is practically the same. Hydraulic loads do not have significant impact on the spherical valve closing time.

References

[1] **Chaudhry, M. Hanif,** 1987, *Applied Hydraulic Transients,* Van Nostrand Reinhold Company, New York.

[2] **Wylie, E. Benjamin and Streeter, L. Victor,** 1993, *Fluid Transients in Systems*, Prentice Hall, Englewood Cliffs.

[3] **Bergant, Anton and Sijamhodžić, Esad,** 1994, *Hydraulic transients caused by shutoff valves*, Conference on Hydropower plants, Budapest, Hungary, pp. 331–341.

---

[4] **Karadžić, Uroš, Bergant, Anton, Vukoslavčević, Petar,** 2010, *Water hammer caused by closure of turbine safety spherical valves*. 25th IAHR Symposium on Hydraulic Machinery and Systems, Timisoara, Romania.

[5] **Karadžić, Uroš, Bergant, Anton, Vukoslavčević, Petar,** 2009, *A novel Pelton turbine model for water hammer analysis*, Strojniški Vestnik – Journal of Mechanical Engineering, Vol.55, No.6, pp. 369–380.

Nomenclature

(Symbols)	(Symbol meaning)
A	Pipe area
A_v	Valve area
a	Pressure wave speed
D	Pipe diameter, diameter
D_v	Nominal valve diameter
F	Darcy-Weisbach friction factor
G	Gravitational acceleration
H	Piezometric head, head
H_d	Head downstream of the valve
H_u	Head upstream of the valve
J	Moment of inertia
K_D	Valve discharge coefficient
L	Length
n	Rotational speed
Q	Discharge
Q_u	Discharge through the valve
T	Torque
t	Time
t_c	Valve closure time
x	Distance along the pipe
z	Water level, elevation
Θ	Angle of the valve opening
(Subscripts)	(Subscripts meaning)
max	Maximum
r	Rated conditions
v	Valve axis
(Abbreviations)	(Abbreviations meaning)
HPP	Hydro Power Plant

Acknowledgments

The authors wish to thank Ministry of Science, Montenegro and ARRS (Slovenian Research Agency) for their support on this research conducted through the project “Measurement of turbulent flow characteristics in pipes and channels”. The support of research by ZAMTES (Montenegrin Bureau for International Scientific, Educational, Cultural and Technical Cooperation) is also gratefully acknowledged.

JET Volume 4 (2011), p.p. 55-72

Issue 2, May 2011

http://www.fe.uni-mb.si/si/jet.html

DETERMINATION OF EQUIVALENT CIRCUIT PARAMETERS FOR THREE-PHASE INDUCTION MOTORS: PROCEDURE IN ACCORDANCE WITH THE IEC 60034-28 STANDARD

DOLOČITEV PARAMETROV NADOMESTNEGA VEZJA TRIFAZNEGA ASINHRONSKEGA MOTORJA PO STANDARDU IEC 60034-28

Matej Mlakar[✉,1], Miralem Hadžiselimović [1,2], Bojan Štumberger [1,2], Ivan Zagradišnik [1]

Keywords: three-phase induction motors, parameters of equivalent circuit

Abstract

Currently, an increasing number of induction motors are being used in liaison with converters, and it is necessary to know the equivalent circuit parameters of the induction motor. In this article, we have calculated equivalent circuit parameters based on the measurement as presented in IEC 60034-28. To evaluate the parameters' results calculated based on the IEC 60034-28 standard, a comparison is made with a calculation from the emLook analytical software package.

✉Corresponding author: Matej Mlakar, BS (Eng.), Bartec Varnost d.o.o., Cesta 9. avgusta 59, 1410 Zagorje ob Savi, E-mail address: matej.mlakar84@gmail.com

[1] Faculty of Electrical Engineering and Computer Science, University of Maribor, Slovenia

[2] Faculty of Energy Technology, University of Maribor, Slovenia

---

Povzetek

V današnjem času se vedno več asinhronskih motorjev uporablja v navezi s pretvornikom in zato je potrebno poznati parametre nadomestnega vezja asinhronskega motorja. V tem članku smo zato izračunali parametre nadomestnega vezja na podlagi meritev, ki so predstavljene v standardu IEC 60034-28. Za oceno pridobljenih parametrov po standardu smo parametre nadomestnega vezja izračunali še z uporabo analitičnega izračuna z računalniškim paketom emLook.

1 INTRODUCTION

Nowadays in various industries, a need for motor regulation has appeared. For motors connected with converters, synchronous motors with permanent magnets are mainly used. Because of the rapid increase in price, permanent magnet synchronic motors are being replaced by induction motors, which are more easily affordable. Induction motors take precedence over synchronous motors even when the operation of the engine may experience short term overload. If the permanent magnets in the synchronous motor experience a short term overload, the magnets demagnetise; hence, the motor's performance decreases. However, when an induction motor experiences short term overloads, the motor continues to function. Regulation requires knowing the equivalent circuit diagram for motors; therefore, we defined the equivalent circuit parameters, according to IEC 60034-28, [2] and then evaluated the results with the emLook software package [4]. The IEC procedure is presented in Section 2.

2 PRESENTATION OF THE IEC PROCEDURE FOR DETERMINING PARAMETERS OF AN EQUIVALENT CIRCUIT

In order to change the speed or torque of an induction motor with a converter, the parameters of an equivalent circuit must be determined. In this article, many equivalent circuits are represented, which all are determined based on the equivalent circuit which is shown in Figure 1 and in accordance with standard IEC 60034-28, [2] which (in this paper) is how the parameters of equivalent circuits are determined. In Figure 1, U_s is the voltage on a stator winding, I_s is the stator phase-current, R_s is the stator phase-resistance, $X_{\sigma s}$ is the stator leakage reactance, U_m is the voltage drop over the magnetising reactance, I_m is the magnetising current, X_m is the magnetising reactance, R_{Fe} is the equivalent resistance of iron losses, I_{Fe} is the equivalent iron losses current, I_r' is the rotor current, $X_{\sigma r}'$ is the rotor leakage reactance, R_r' is the rotor resistance and s is the slip.

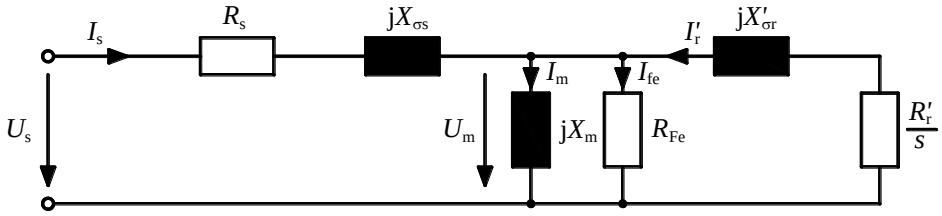

Figure 1: *Equivalent circuit diagram of the induction motor.*

To determine the parameters of the equivalent circuit, a type 4KTC 112 M4 motor is used. More about this motor is discussed in Section 3. To determine the parameters of the equivalent circuit, the no-load test, load test and locked rotor test are presented in Sections 4.2 to 4.4. For measuring the motor, a measuring set up is needed, which is presented in Section 4.1. The parameters for the equivalent circuit, determined according to the IEC standard, are presented in Section 5. In Section 6, parameters are determined using the emLook software package to evaluate the results obtained according to the IEC standard.

3 PRESENTATION OF THE TYPE 4KTC 112 M-4 MOTOR

Here is the data for the motor used in the determination of parameters of the equivalent circuit: output power $P_2 = 4\,\text{kW}$, rated voltage U_N, rated current I_N, power factor $\cos\varphi$, speed n and rated torque M_N written below:

$P_2 = 4\,\text{kW}$ $U_N = \Delta\ 400\ \text{V}$ $I_N = 8{,}2\ \text{A}$ $\cos\varphi = 0{,}84$ $n = 1430\ \text{min}^{-1}$ $M_N = 26{,}8\ \text{Nm}$

More detail information about the type 4KTC 112 M4 motor is given on the Bartec Varnost (the motor's manufacturer) website [5]. The shaft height of this motor is 112 mm.

Every induction motor consists of two cylinders, with one fitted within another and enclosed by a grey cast iron frame. The inner cylinder is called the rotor and the outer cylinder is called the stator. Both are assembled with multiple laminated sheets so that the occurrence of eddy currents losses is limited. The laminated sheet has a thickness of 0,5 mm and has iron losses of 5,55 W/kg at an induction of 1,5 T. The slots are stamped on the inner area of the lamellas of a stator; in contrast the slots on the lamellas on the rotor where are stamped in the outer area. Figures 2 and 3 show the shape of the stator and rotor slots. For more information about the stator and rotor slots, please see the Kienle & Spiess product catalogue, under product number IEC 112/4.103 [6].

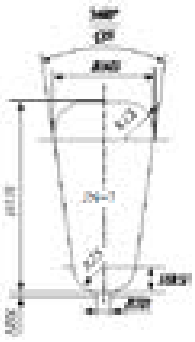

Figure 2: *Picture of stator slot*

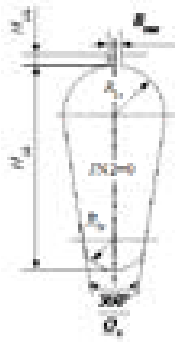

Figure 3: *Picture of rotor slot*

The copper winding is inserted in the stator slots; in this case, a three-phase single layer concentric winding with a coil pitch of 1–8, 10, 12. A schematic diagram of this winding is shown in Figure 4.

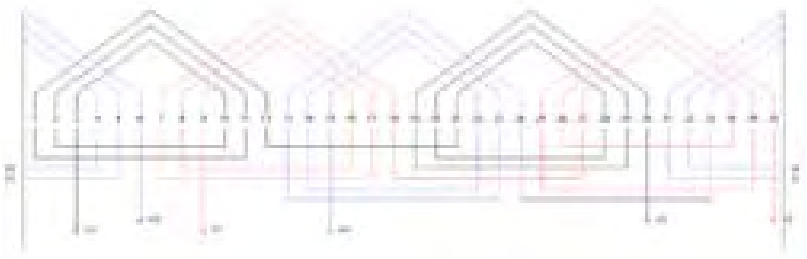

Figure 4: *Stator single layer concentric winding with coil pitch 1–8, 10, 12, [3].*

In the rotor, the squirrel cage is made of aluminium. Further information on this rotor can be found in the Kienle & Spiess product catalogue, under product number 72.650.

After selecting the test motor, the load test, no-load test and the locked rotor test are done. These tests are presented in the following section.

4 DESCRIPTION OF MEASUREMENTS ACCORDING TO THE IEC 60034-28 STANDARD

For the calculation of the equivalent circuit parameters according to IEC 60034-28, [2], it is necessary to measure the load-test, no-load test and locked rotor test of the induction motor. The motor, type 4KTC 112 M-4, was manufactured by the company Bartec Varnost. For measurement, we used the measuring set up which is presented in Section 4.1.

4.1. Measuring set up

The measuring set up consists of an autotransformer, electrical power plant, frequency convertor, Norma power analyser, induction motor, DC amplifier, torque transducer and computer. With the autotransformer or electrical power plant, the level of voltage supply in the motor can be changed. Another part of the measuring set up is the frequency convertor, which controls the dynamometer that serves as a brake. To measure the voltage, the current and the power, we use a NORMA power analyser, which is connected to a PC. To measure the torque, we used a torque sensor that is connected to a NORMA power analyser. The measuring set up is shown in Figure 5.

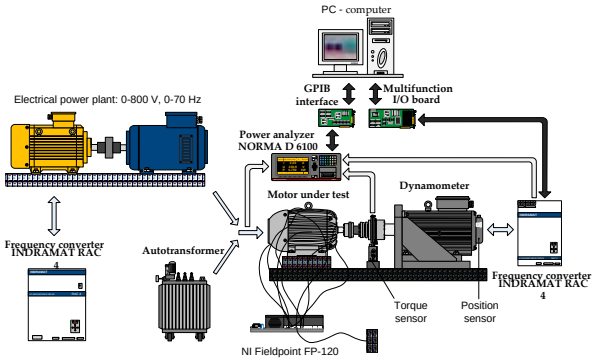

Figure 5: *Measuring set up.*

First the load test is done; the procedure of testing is presented in Section 4.2.

4.2. The load test of the induction motor according to the IEC 60034-28 standard

Before testing the induction motor, we measured the resistance of the winding and the temperature of the induction motor. On the basis of these measurements, we set the resistance of the winding at 25 °C, as recommended by the IEC 60034-28 standard [2].

After these resistance measurements, the test of the induction motor load according to the IEC 60034-28 standard [2] was made. During this test, we considered a ±5 °C deviation of the temperature from the predetermined temperature, which in our case was 90 °C. Figure 6 shows the graphs of speed, power factor, current and input power that are based on the measurements of the load test for the type 4KTC 112 M-4 induction motor. Figure 6 illustrates how to obtain the speed, power factor, current and input power at the rated torque that is determined from the characteristic of output power P_2 at the rated power $P_N = 4$ kW . The obtained values of speed n, power factor $\cos\varphi$, current I and input power P_1 at the rated torque are given in a Table 1. In Table 2, the measured temperature of the winding ϑ_0, stator winding resistance $R_{s,23}$ at the initial temperature and the after load test measured temperature of winding ϑ_{ob} and stator winding resistance $R_{s,90}$ are given.

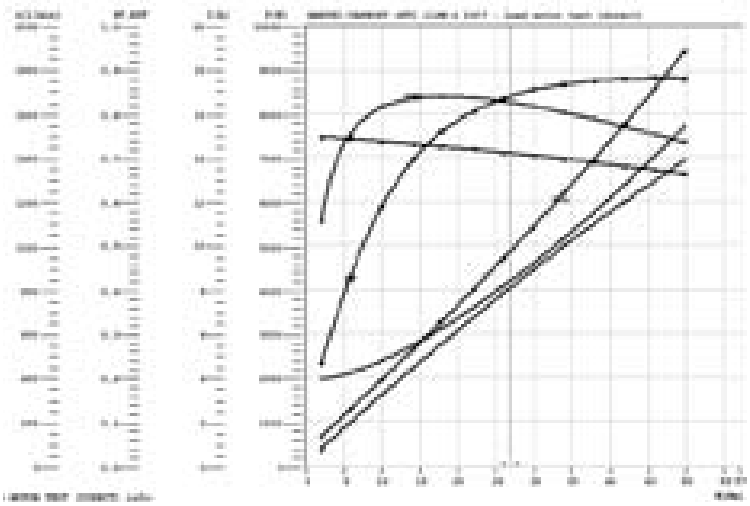

Figure 6: *Characteristics of load motor test.*

Table 1: *Results from characteristics at rated output power.*

U (V)	I (A)	P_1 (W)	cosφ	M (Nm)	n (min^{-1})	P_2 (W)
400,5	8,31	4839	0,84	26,9	1420,1	4000

Table 2: *The temperature and resistance of cooled winding and after a load test measured temperature and resistance.*

$R_{s,23}$ (Ω)	ϑ_0 (°C)	$R_{s,90}$ (Ω)	ϑ_{ob} (°C)
2,3258	23	2,931	90,13

When the load test is done the no-load test begins. This test is represented in the following Section 4.3

4.3. The no-load test of the induction motor according to the IEC 60034-28 standard

In this test, the shaft on the measured motor is not loaded; only the voltage on the stator has been changed. The measurements need to be performed at least ten different voltages. The highest measuring voltage for the measured motor, according to the IEC 60034-28 standard [2] shall not be lower than 110% of the rated voltage. The IEC 60034-28 standard [2] recommends the lowest measuring voltage of the no-load to be 20% of the rated voltage. The no-load measurement is initially taken at the highest voltage, which is then subsequently lowered. Figure 7 shows the characteristic of the power factor, the characteristic of current and the characteristic of input power based on measurements. Along with this, it shows how to obtain the power factor, current and input factor at the rated voltage $U_n = 400$ V from the graph. The

power factor, current and input power at the rated voltage is shown in Table 3. In Table 4, the measured temperature of the winding ϑ_0 and stator winding resistance $R_{s,23}$ at the initial temperature and the following no-load test measured temperature of winding ϑ_{pt} and stator winding resistance $R_{s,27}$ are given.

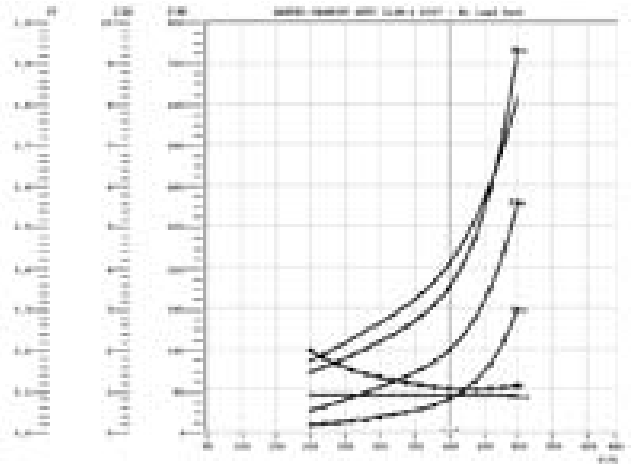

Figure 7: *Characteristics of the no-load motor test.*

Table 3: *Characteristics results at rated voltage.*

U (V)	I (A)	P_1 (W)	cosφ
400	4,02	276	0,099

Table 4: *The temperature and resistance of the cooled winding and after a no-load test measured temperature and resistance.*

$R_{s,23}$ (Ω)	ϑ_0 (°C)	$R_{s,27}$ (Ω)	ϑ_{pt} (°C)
2,3258	23	2,365	27,35

For the no-load test, the equivalent circuit diagram is changed, as shown in Figure 8. Because the rotor current is negligible, the rotor current is disregarded.

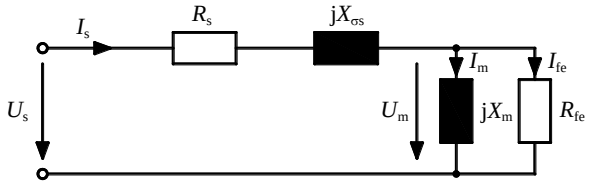

Figure 8: *Equivalent circuit diagram of the induction motor for a no-load test.*

After the no-load test, the locked rotor test is measured, which is presented in Section 4.4.

4.4. The locked rotor test of the induction motor according to the IEC 60034-28 standard

The final test conducted was the locked rotor test of the type 4KTC 112 M-4 induction motor. The standard sets the possibility of measuring counter results of the reverse rotating test as well as the locked rotor. However, we did not choose to do the reverse rotation test. While conducting the locked rotor test, the rotor is mechanically blocked. The measurement needs to be made at a lower voltage so that the motor is not destroyed. First, a run through is done to obtain measurements with the voltage being increased to the point of the highest current decided. Afterwards, the measurements are taken for the rest of the predetermined currents. The IEC 60034-28 Standard [2] recommends the highest measured current measuring to be 150% of the rated current. The lowest value of the current recommended by the standard is 10% of the rated current. The characteristics that are shown in Figure 9 are plotted on the basis of measurements of the locked rotor test. Table 5 shows the obtained power factor, torque, voltage and input power from the characteristic in Figure 9 at the rated current $I_N = 8{,}31$ A . In Table 6, the measured temperature of the winding ϑ_0 and the stator winding resistance $R_{s,23}$ at the initial temperature and the after the locked rotor test measured temperature of winding ϑ_{KS} and stator winding resistance $R_{s,95}$ are given.

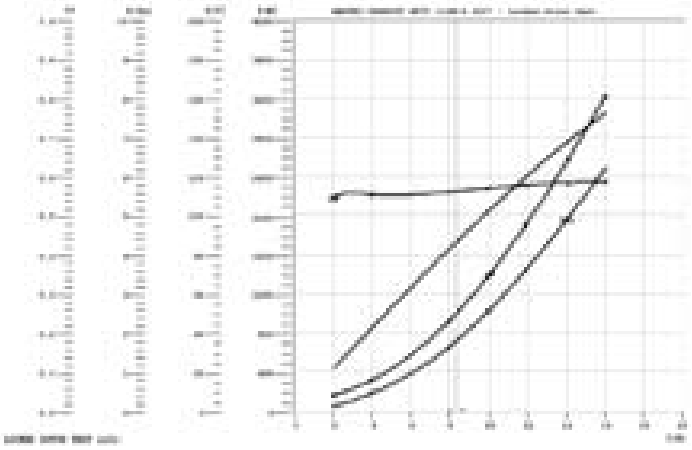

Figure 9: *Characteristics of the locked rotor test.*

Table 5: *Characteristics results at the rated current.*

U (V)	I (A)	P_1 (W)	cosφ	M (Nm)
85,2	8,31	687	0,56	2,42

Table 6: *The temperature and resistance of the cooled winding; and measured temperature and resistance after the no-load test.*

$R_{s,23}$ (Ω)	ϑ_0 (°C)	$R_{s,95}$ (Ω)	ϑ_{ks} (°C)
2,3258	23	2,975	95,02

For the locked rotor test, the equivalent circuit diagram is changed as shown in Figure 10. Because the rotor and stator currents are high compared with the magnetising current, the magnetising current is disregarded.

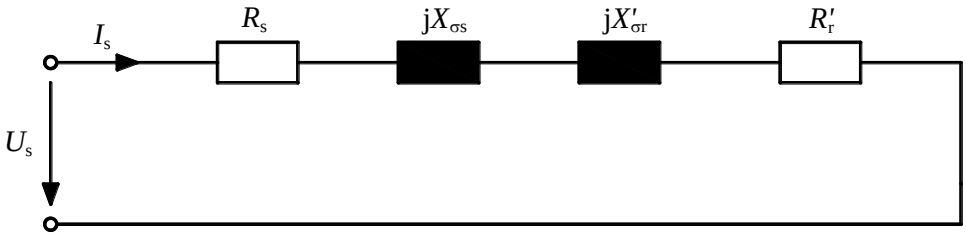

Figure 10: *Equivalent circuit diagram of the induction motor for the locked rotor test.*

When all tests are complete, the parameters of the equivalent circuit are determined based on the IEC standard as presented in Section 5.

5 THE DETERMINATION OF PARAMETERS OF EQUIVALENT CIRCUIT BASED ON IEC 60034-28 STANDARD

The calculation of the iron losses P_{Fe} and the equivalent circuit resistance of iron losses R_{Fe} are determined with the measurements of the no-load test. First, the stator phase-resistance, corrected to a temperature of 25 °C $R_{s,25}$, is calculated along the measured stator line-to-line resistance at initial winding temperature $R_{s,23}$ and measured initial winding temperature ϑ_0 according to the Equation 5.1. Then the calculation of the constant losses P_k is made for each point of no-load measurement according to Equation 5.3. Therefore the stator phase-current I_s needs to be calculated according to Equation 5.2 and the temperature of the winding at the end of the thermal no-load test ϑ_{pt} needs to be measured. Then, plotting the first tree point of P_k at the lowest voltages squared U^2 and extrapolating a straight line to zero voltage is done. The intercept with the zero voltage axis is the friction and windage losses P_{trv} that are shown in Figure 11. Finally, the P_{Fe} and then R_{Fe} are calculated according to Equations 5.4 and 5.5.

$$R_{s,25} = \frac{3}{2} \cdot R_{s,23} \cdot \frac{235+25}{235+\vartheta_0} \quad (5.1) \qquad I_s = \frac{I}{\sqrt{3}} \quad (5.2)$$

$$P_k = P_1 - 3 \cdot I_s^2 \cdot R_{s,25} \cdot \frac{235+\vartheta_{pt}}{235+25} \quad (5.3) \qquad P_{Fe} = P_k - P_{trv} \quad (5.4)$$

$$R_{Fe} = \frac{3 \cdot U_s^2}{P_{Fe}} \quad (5.5)$$

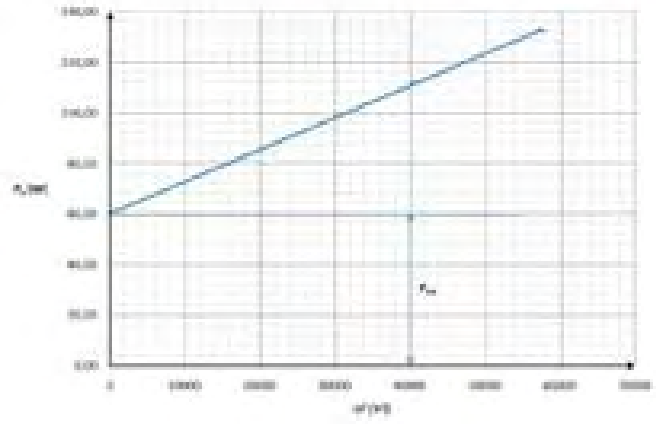

Figure 11: *Characteristic of power P_k against square voltage U^2.*

To calculate the other parameters of the equivalent circuit diagram, the measurements of no-load, load and lock rotor tests are made. First, the calculation of the total leakage $L_{\sigma i}$ inductance is made based on the measurement of lock rotor test. For each of the measured line-currents I, the calculation of motor impedance Z and power factor $\cos\varphi$ following Equations 5.6, 5.7 is done. Next, the calculations of line resistance R, total leakage reactance disregarding the skin-effect $X'_{\sigma i}$ and total leakage inductance disregarding the skin-effect $L'_{\sigma i}$ are done following Equations 5.8, 5.9 and 5.10. Then, the total leakage inductance $L_{\sigma i}$ is calculated regarding the skin effect following Equations 5.11, 5.12, 5.13 and 5.14. Figure 12 shows the plot the values of $L_{\sigma i}$ against the values I.

$$Z = \frac{U\sqrt{3}}{I} \quad (5.6) \qquad \cos\varphi = \frac{P_1}{UI\sqrt{3}} \quad (5.7)$$

$$R = Z\cos\varphi \quad (5.8) \qquad X'_{\sigma i} = \sqrt{Z^2 - R^2} \quad (5.9)$$

$$L'_{\sigma i} = \frac{X'_{\sigma i}}{2\pi f_N} \quad (5.10) \qquad h = \left(0{,}21 - \frac{2p}{100}\right)\frac{H}{1000} \quad (5.11)$$

$$\xi = h\sqrt{\pi f 4\pi 10^{-7} \gamma_r} \quad (5.12) \qquad k_X = \frac{3}{2\xi}\frac{\sinh(2\xi) - \sin(2\xi)}{\cosh(2\xi) - \cos(2\xi)} \quad (5.13)$$

$$L_{\sigma i} = L'_{\sigma i} \frac{k_{\sigma i} + 1}{k_{\sigma i} + k_X} \qquad (5.14)$$

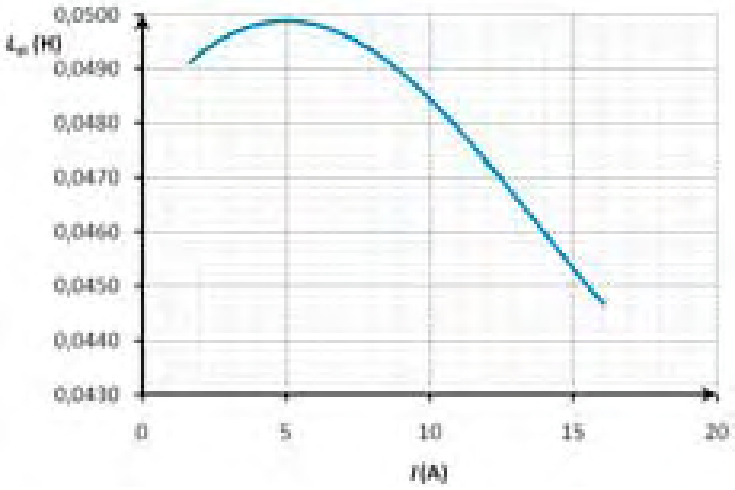

Figure 12: *Characteristic of inductance $L_{\sigma i}$ over current I.*

Based on measurement of the no-load test, the total stator inductance L_s is calculated with the same procedure as the inductance $L'_{\sigma i}$. Figure 13 shows the characteristic of inductance L_s over current I .

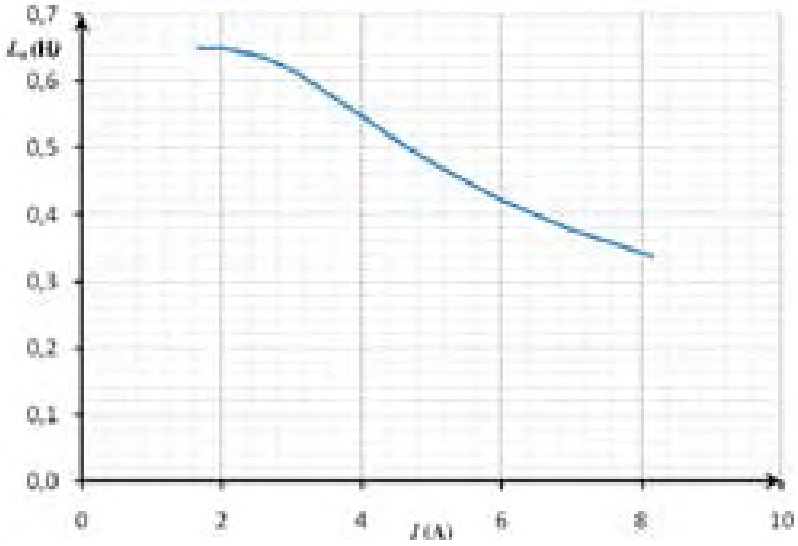

Figure 13: *Characteristic of total stator inductance L_s over current I.*

For each measured line current on the no-load test, the value of $L_{\sigma i}$ is determined as shown in Figure 12. Then, the magnetising inductance L_m, voltage drop over the magnetising inductance U_m, stator leakage inductance $L_{\sigma s}$ and rotor leakage inductance $L'_{\sigma r}$ are calculated for each measured line current, following Equations 5.15, 5.16, 5.17 and 5.18. The motor has a single cage rotor, and therefore the value of $k_{\sigma i}$ in our case is 1, according to the IEC standard. Figures 14, 15 and 16 show the plotted characteristics of inductance L_m, $L_{\sigma s}$ and $L'_{\sigma r}$ based on previous calculations of inductance L_m, $L_{\sigma s}$ and $L'_{\sigma r}$.

$$L_m = L_s - \frac{L_{\sigma i}}{1+\frac{1}{k_{\sigma i}}} \tag{5.15}$$

$$U_m = 2\pi f_N L_m I_m \tag{5.16}$$

$$L_{\sigma s} = L_s - L_m \tag{5.17}$$

$$L'_{\sigma r} = L_{\sigma i} - L_{\sigma s} \tag{5.18}$$

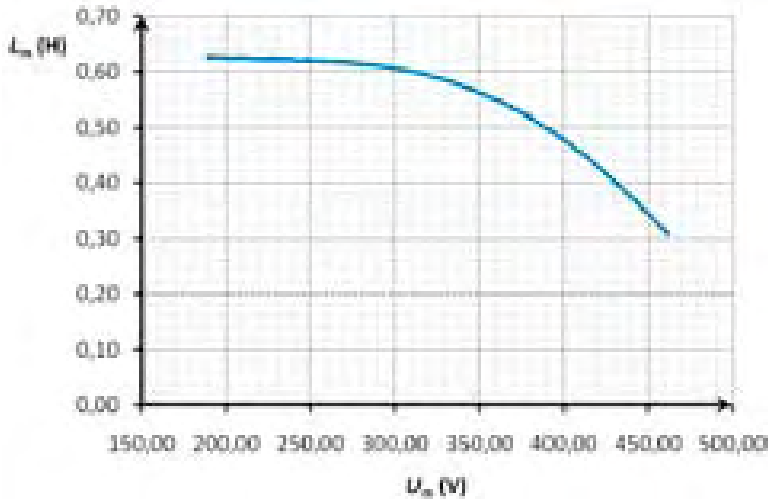

Figure 14: *Characteristic of inductance L_m over voltage U_m.*

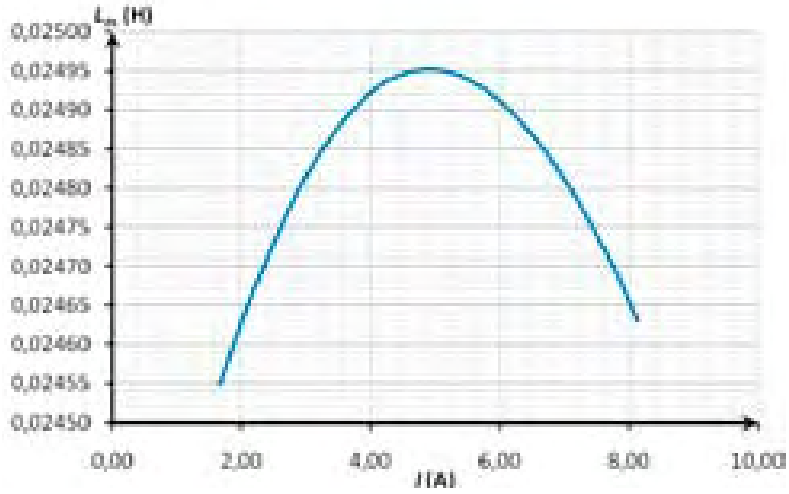

Figure 15: *Characteristic of inductance L_{os} over current I.*

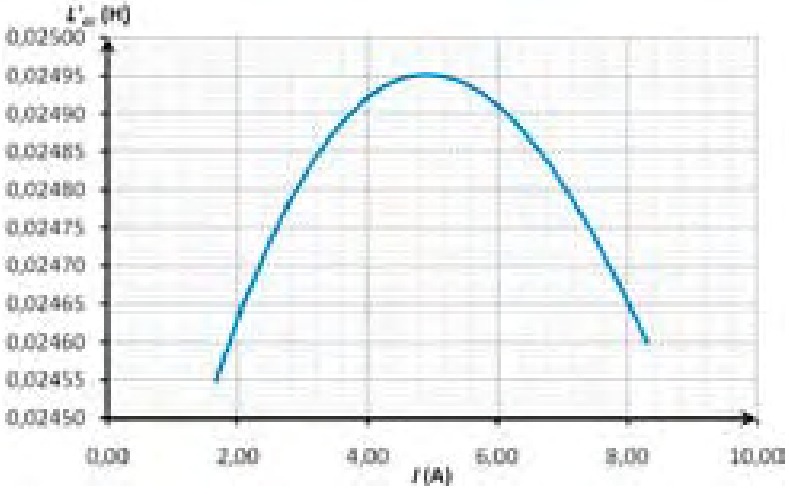

Figure 16: *Characteristic of inductance L'_{or} over current I.*

From the characteristics of the load test, the current is determent at the rated torque. For this current, the values of inductances L_{os} and L'_{or} are determined in Figures 15 and 16. To determine the inductance L_m from Figure 14, the calculation of voltage U_m is made, following Equations 5.19, 5.20, 5.21, 5.22 and 5.23, based on data in Table 1 and the measured temperature of winding at the end of the thermal load test ϑ_{ob}. Then the calculations of the rotor current I'_r, the rotor leakage reactance X'_{or}, the stator leakage reactance X_{os} and the magnetising reactance X_m are made following Equations 5.24, 5.26, 5.27, 5.28 and 5.29. In the end, the calculation of rotor resistance, corrected to an ambient temperature of 25°C, is made, following Equations 5.30.

$$s = \frac{n_s - n}{n_s} \quad (5.19) \qquad \cos\varphi = \frac{P_1}{UI\sqrt{3}} \quad (5.20)$$

$$U_{ma} = U_s - I_s\left(\cos\varphi R_{s,25}\frac{235+\vartheta_{ob}}{235+25} + \sqrt{1-(\cos\varphi)^2}\,2\pi f_N L_{\sigma s}\right) \quad (5.21)$$

$$U_{mb} = I_s\left(\sqrt{1-(\cos\varphi)^2}R_{s,25}\frac{235+\vartheta_{ob}}{235+25} - \cos\varphi 2\pi f_N L_{\sigma s}\right) \quad (5.22)$$

$$U_m = \sqrt{U_{ma}^2 + U_{mb}^2} \quad (5.23) \qquad Z = \frac{U\sqrt{3}}{I} \quad (5.24)$$

$$I_r' = \sqrt{\left(\frac{U_{mb}}{2\pi f_N L_m} - I_s\cos\varphi\right)^2 + \left(I_s\sqrt{1-(\cos\varphi)^2} - \frac{U_{ma}}{2\pi f_N L_m}\right)^2} \quad (5.25)$$

$$X = Z\sqrt{1-(\cos\varphi)^2} \quad (5.26) \qquad X_{\sigma r}' = 2\pi f_N L_{\sigma r}' \quad (5.27)$$

$$X_{\sigma s} = 2\pi f_N L_{\sigma s} \quad (5.28) \qquad X_m = 2\pi f_N L_m \quad (5.29)$$

$$R_{r,25}' = s\left(X_r' + X_m\right)\sqrt{\frac{\frac{X_m X_r'}{X_m + X_r'} - \left(X - X_s\right)}{X - X_s - X_m}}\,\frac{225+25}{225+\vartheta_{ob}} \quad (5.30)$$

Table 7 shows the determined parameters of the equivalent circuit based on the IEC 60034-28 standard.

Table 7: *Parameters determinate based on the IEC 60034-28 standard.*

	$R_{s,25}$ (Ω)	$R'_{r,25}$ (Ω)	R_{Fe} (Ω)	$X_{\sigma s}$ (Ω)	$X'_{\sigma r}$ (Ω)	X_m (Ω)
The determined parameters according to IEC 60034-28	3,516	3,598	3144,02	7,728	7,728	171,22

To evaluate the results of the determined parameters of the equivalent circuit diagram in accordance with the IEC 60034-28 standard, a comparison with determined parameters derived from the emLook software package is made. In Section 6, a short presentation of the software and the results are given.

6 THE DESCRIPTION OF THE EMLOOK SOFTWARE PACKAGE

The emLook software package [4] is used for the design of electric motors. Based on the data on the induction motor that is presented in Section 3, the calculation of the data for the no-load, locked rotor and load motor is made, while the software also calculates the parameters of the equivalent circuit as shown in Table 8. More information about the software package can be found in the article listed in the reference section [4].

Table 8: *Parameters determined with the emLook software package.*

	$R_{s,25}$ (Ω)	$R'_{r,25}$ (Ω)	R_{Fe} (Ω)	$X_{\sigma s}$ (Ω)	$X'_{\sigma r}$ (Ω)	X_m (Ω)
The determined parameters with the emLook software package	3,510	3,390	3172,50	6,200	7,130	177,24

7 CONCLUSION

In this article, we have made calculations of equivalent circuit parameters with two methods. The first method is based on measurements and is presented based on the IEC 60034-28 standard. The other approach is by using results from the calculations generated by the emLook analytical software. Equivalent circuit parameters calculated according to IEC [2] differ minutely from the calculations made with the emLook software package. Significant variations occur in the calculation of leakage reactance, because (until now) we could not adequately evaluate the additional losses in the measurements. The method that included calculations according to IEC did not consider additional losses and it did not properly consider the iron saturation in the locked rotor test; therefore, the results obtained by this method are not the most accurate. Nevertheless, the method based on the IEC standard is suitable for determining the equivalent circuit parameters, because the results obtained by both methods have minimal differences in stator resistance (0,2%), in rotor resistance (5,8%), in the equivalent circuit resistance of iron losses (0,9%), and in magnetising reactance (3,5%). Exceptions where there are significant differences are in stator leakage reactance (19,8%) and in rotor leakage reactance (7,7%).

References

[1] **Ivan Zagradišnik, Bojan Slemnik:** *Električni rotacijski stroji,* Tiskarna Tehniških fakultet Maribor, p.p. 77-156, 2007

[2] IEC 60034-28 Ed.1: *Rotating electrical machines – Part 28: Test methods for determining quantities of equivalent circuit diagrams for tree-phase low-voltage cage induction motors,* p.p. 1-28, 2007

[3] **Boštjan Gajšek, Miralem Hadžiselimović:** *Segrevanje protieksplozijskega asinhronskega motorja pri frekvenci napajalne napetosti 50 in 60 Hz*, diploma, UM FERI, p.p. 1–73, 2009

[4] **Ivan Zagradišnik, Miralem Hadžiselimović, Jože Ritonja, Bojan Slemnik:** *The emLook software package for the analytical and numerical analyses of electrical machines ,* Electrical review, p.p. 175–178, 2010

[5] Bartec Varnost Website: http://www.bartec-varnost.si/katalog/index.php?lang=eng

[6] Kienle & Spiess Website: http://katalog.kienle-spiess.de/index.cfm

---

Nomenclature

(Symbols)	(Symbol meaning)
$\cos\varphi$	Power factor
f	Frequency
h	The height of the rotor-conductor bar
H	Motor frame size according to IEC 60072-1 (shaft height)
I	Stator line-current
I_s	Stator phase-current
I'_r	Rotor current
I_m	Magnetising current
k_x	Skin-effect factor for inductance
$k_{\sigma i}$	Ratio of stator to rotor leakage inductance
L_m	Magnetising inductance
$L_{\sigma s}$	Stator leakage inductance
$L'_{\sigma r}$	Rotor leakage inductance
$L_{\sigma i}$	Total leakage inductance
$L'_{\sigma i}$	Total leakage inductance, disregarding the skin effect
L_s	Total stator inductance
M	Torque
n	Operating speed
n_s	Rated synchronous speed
p	Number of pole pairs
P_1	Electrical input power
P_2	Electrical output power
P_{Cu}	Winding losses
P_{Fe}	Iron losses
P_k	The constant losses
P_{trv}	Windage and friction losses
R	The line resistance
R_{Fe}	Equivalent circuit resistance of iron losses

R_{L1-L2}	The stator line to line resistance at initial winding temperature
R'_r	Rotor cage resistance
$R_{r,25}'$	Rotor cage resistance corrected to a temperature of 25 °C
R_s	Stator phase- resistance
$R_{s.25}$	Stator phase- resistance corrected to a temperature of 25 °C
s	Slip
U	Stator terminal voltage
U_s	Stator phase-voltage
U_m	A voltage drop over the magnetising inductance
U_{ma}	A voltage component used for calculations
U_{mb}	A voltage component used for calculations
X_m	The magnetising reactance
$X'_{\sigma r}$	Rotor leakage reactance
$X_{\sigma s}$	Stator leakage reactance
$X_{\sigma i}$	The total leakage reactance
$X'_{\sigma i}$	The total leakage reactance disregarding the skin effect
X_s	The total stator reactance
Z	Motor impedance
γ_r	The conductivity of rotor conductor
ξ	The current displacement factor of rotor conductor
ϑ_0	The temperature of the cold winding at initial resistance measurement
ϑ_{ob}	The temperature of the winding at the end of thermal load test
ϑ_{pt}	The temperature of the winding at the end of thermal no-load test

http://www.fe.uni-mb.si/si/jet.html

AUTHOR INSTRUCTIONS (MAIN TITLE)

SLOVENIAN TITLE

Authors, Corresponding author[ℜ]

Key words: (Up to 10 keywords)

Abstract

Abstract should be up to 500 words long, with no pictures, photos, equations, tables, only text.

Povzetek

(In Slovenian language)

Submission of Manuscripts: All manuscripts must be submitted in English by e-mail to the editorial office at jet@uni-mb.si to ensure fast processing. Instructions for authors are also available online at www.fe.uni-mb.si/si/jet.html.

Preparation of manuscripts: Manuscripts must be typed in English in prescribed journal form (Word editor). A Word template is available at the Journal Home page.

A title page consists of the main title in the English and Slovenian languages; the author(s) name(s) as well as the address, affiliation, E-mail address, telephone and fax numbers of author(s). Corresponding author must be indicated.

Main title: should be centred and written with capital letters (ARIAL **bold** 18 pt), in first paragraph in English language, in second paragraph in Slovenian language.

Key words: A list of 3 up to 6 key words is essential for indexing purposes. (CALIBRI 10pt)

Abstract: Abstract should be up to 500 words long, with no pictures, photos, equations, tables, - text only.

Povzetek: - Abstract in Slovenian language.

[ℜ] Corresponding author and other authors: Title, Name and Surname, Tel.: +XXX x xxx xxx, Fax: +XXX x xxx xxx, Mailing address: xxxxxxxxxxxxxxxxxxxxxxxxxxxxxxxxx, E-mail address: email@xxx.xx

---

Main text should be structured logically in chapters, sections and sub-sections. Type of letters is Calibri, 10pt, full justified.

Units and abbreviations: Required are SI units. Abbreviations must be given in text when firstl mentioned.

Proofreading: The proof will be send by e-mail to the corresponding author, who is required to make their proof corrections on a print-out of the article in pdf format. The corresponding author is responsible to introduce corrections of data in the paper. The Editors are not responsible for damage or loss of manuscripts submitted. Contributors are advised to keep copies of their manuscript, illustrations and all other materials.

The statements, opinions and data contained in this publication are solely those of the individual authors and not of the publisher and the Editors. Neither the publisher nor the Editors can accept any legal responsibility for errors that could appear during the process.

Chapter examples:

1 MAIN CHAPTER

(Arial bold, 12pt, after paragraph 6pt space)

1.1 Section

(Arial bold, 11pt, after paragraph 6pt space)

1.1.1 Sub-section

(Arial bold, 10pt, after paragraph 6pt space)

Example of Equation (lined 2 cm from left margin, equation number in normal brackets (section.equation number), lined right margin, paragraph space 6pt before in after line):

$$c = \sqrt{a^2 + b^2} \tag{1.1}$$

Tables should have a legend that includes the title of the table at the top of the table. Each table should be cited in the text.

Table legend example:

Table 1: *Name of the table (centred, on top of the table)*

Figures and images should be labelled sequentially numbered (Arabic numbers) and cited in the text – Fig.1 or Figure 1. The legend should be below the image, picture, photo or drawing.

Figure legend example:

Figure 1: *Name of the figure (centred, on bottom of image, photo, or drawing)*

References

[1] **Name. Surname:** *Title,* Publisher, p.p., Year of Publication

Example of reference-1 citation: In text, Predin, [1], text continue. **(Reference number order!)**

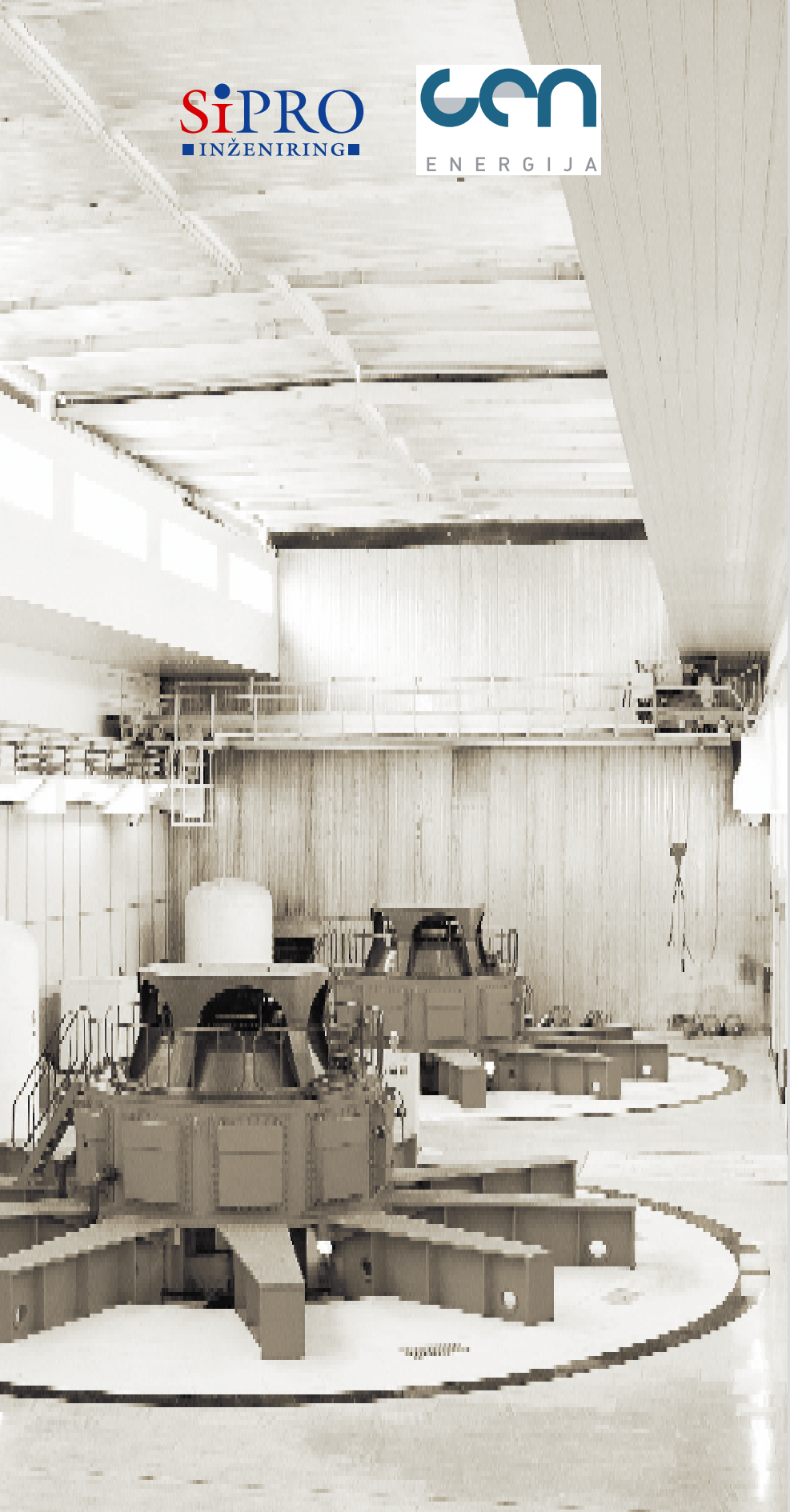

SiPRO INŽENIRING

GEN ENERGIJA

JET

JET Journal of ENERGY TECHNOLOGY Vol. 4/2 2011 UNIVERSITY OF MARIBOR, FACULTY OF ENERGY TECHNOLOGY

9 771855 574008

ISSN 1855-5748